**Article:**

Wang, S, Nissen, E, Pousse-Beltran, L et al. (3 more authors) (2022) Structural controls on Coseismic rupture revealed by the 2020 Mw 6.0 Jiashi earthquake (Kepingtag belt, SW Tien Shan, China). Geophysical Journal International. ggac159. ISSN 0956-540X

https://doi.org/10.1093/gji/ggac159

# Structural controls on coseismic rupture revealed by the 2020 $M_w$ 6.0 Jiashi earthquake (Kepingtag belt, SW Tian Shan, China)

Siyu Wang[1⋆], Edwin Nissen[1], Léa Pousse-Beltran[1,2], Timothy J. Craig[3], Ruohong Jiao[1], and Eric A. Bergman[4]

[1]*School of Earth and Ocean Sciences, University of Victoria, Victoria*V8P 5C2*, British Columbia, Canada*

[2] *Institute des Sciences de la Terre, Université Grenoble Alpes, 38058 Grenoble, France*

[3] *School of Earth and Environment, COMET, Institute of Geophysics and Tectonics, University of Leeds, Leeds, UK*

[4] *Global Seismological Services, Golden, CO 80401, USA*

8 April 2022

**SUMMARY**

The Kepingtag (Kalpin) fold-and-thrust belt of the southern Chinese Tian Shan is characterized by active shortening and intense seismic activity. Geological cross-sections and seismic reflection profiles suggest thin-skinned, northward-dipping thrust sheets detached in an Upper Cambrian décollement. The January 19 2020 $M_w$ 6.0 Jiashi earthquake provides an opportunity to investigate how coseismic deformation is accommodated in this structural setting. Coseismic surface deformation resolved with Sentinel-1 Interferometric Synthetic Aperture Radar (InSAR) is centered on the back limb of the frontal Kepingtag anticline. Elastic dislocation modelling suggests that the causative fault is located at ∼7 km depth and dips ∼7° northward, consistent with the inferred position of the décollement. Our calibrated relocation of the mainshock hypocenter is consistent with eastward, unilateral rupture of this fault. The narrow slip pattern (length ∼37 km but width only ∼9 km) implies that there is a strong struc-

tural or lithological control on the rupture extent, with up-dip slip propagation possibly halted by an abrupt change in dip angle where the Kepingtag thrust is inferred to branch off the décollement. A depth discrepancy between mainshock slip constrained by InSAR and teleseismic waveform modelling (∼7 km) and well-relocated aftershocks (∼10–20 km) may suggest that faults within sediments above the décollement exhibit velocity-strengthening friction.

**Key words:**

Radar interferometry, Asia, Earthquake source observations, Waveform inversion, Folds and folding, Intra-plate processes

## 1 INTRODUCTION

Late Cenozoic crustal deformation in central Asia is dominated by reverse and strike-slip faulting and folding within and around the margins of the Tian Shan mountains. Geodetic data indicate that ∼6–9 mm/yr of the present-day shortening occurs across the Chinese Tian Shan between the northwestern Tarim Basin and southern Kyrgyzstan (Reigber et al., 2001; Wang et al., 2020). The Kepingtag (Kalpin) fold-and-thrust belt has developed along part of the southern margin of this range (Fig. 1). This actively-deforming belt is one of the most earthquake-prone regions of the Tian Shan and of China. In recent years, this intense seismicity has attracted much interest in the deformation style, rate and other characteristics of the Kepingtag belt (Allen et al., 1999; Zhou & Xu, 2000; Zhang et al., 2008; Yang et al., 2002, 2006; Ran et al., 2006). Furthermore, it is one of the few parts of Tian Shan where deformation can be seen stepping into the surrounding foreland, with emergent thrust sheets predominantly vergent toward the Tarim basin in the south. Therefore, the deformation of the Kepingtag belt can also inform how the mountain ranges of southern Tian Shan grow through time.

Fold-and-thrust belts pose distinct challenges for seismic hazard assessment since much of the active faulting is buried. This is exemplified by iconic earthquakes such as the 1978 $M_s$ 7.4 Tabas, Iran earthquake (Walker et al., 2003) and the 1987 $M_w$ 5.9 Whittier and 1994 $M_w$ 6.7 Northridge, California earthquakes (e.g., Davis et al., 1989; Jones et al., 1994), each characterized

⋆ GJI

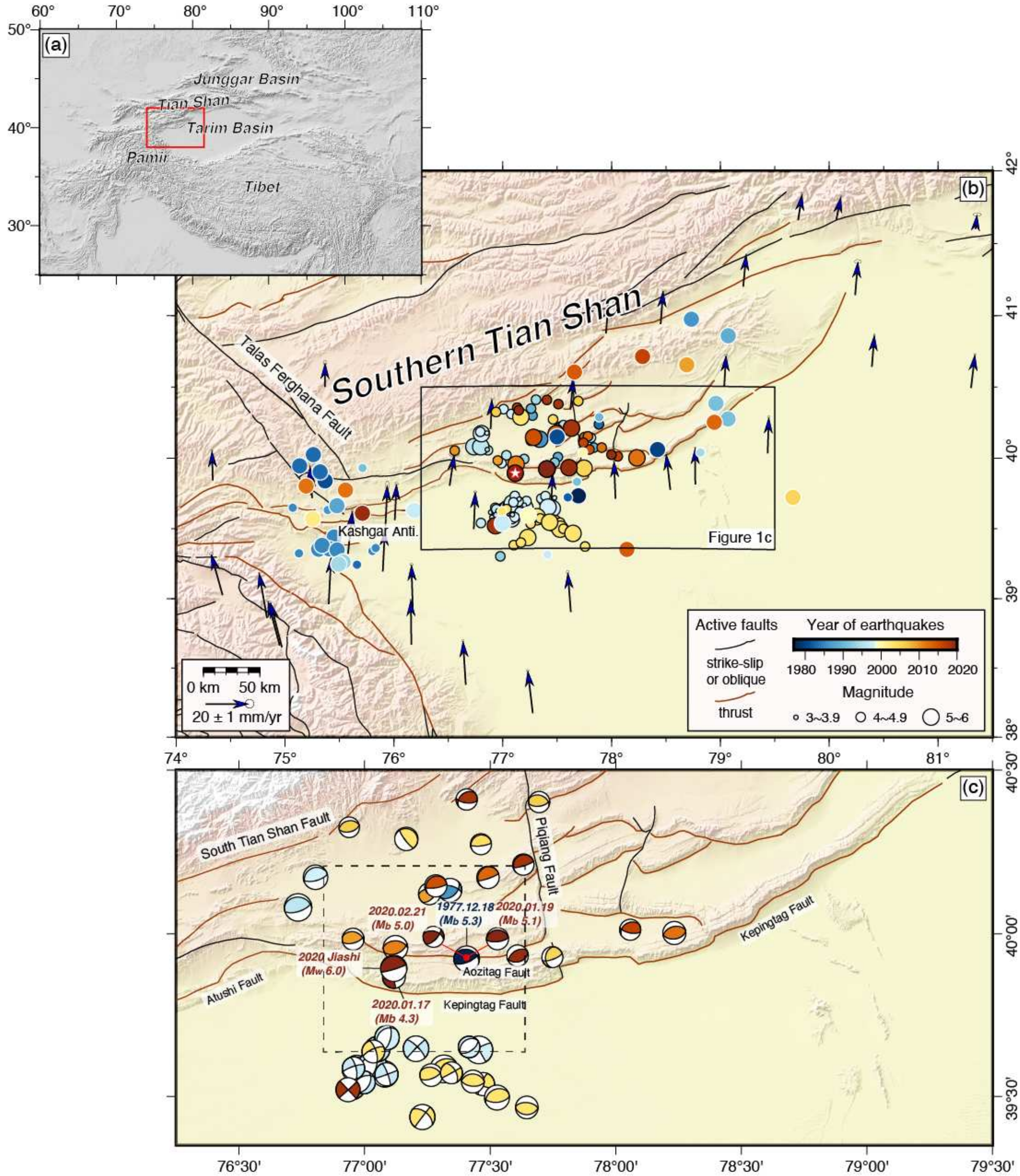


**Figure 1.** Tectonics and seismicity of the study area. (a) Shaded relief of the Himalayan orogeny with the location of panel (b) outlined in red. (b) Tectonic map of the southern Tian Shan. Instrumental seismicity is scaled by magnitude and colored by year from 1977.12.18 to 2020.02.21. Our own relocated epicenters are shown with black outlines, while those from the United States Geological Survey (USGS) have white outlines. The white star is the relocated epicenter of the 2020 January 19 Jiashi mainshock. Active faults are from the online database provided by the Institute of Geology, China Earthquake Administration (http://www.neotectonics.cn/arcgis/apps/webappviewer/index.html?id=3c0d8234c1dc43eaa0bec3ea03bb00bc) and Global Navigation Satellite Systems (GNSS) velocities relative to stable Eurasia are from Wang et al. (2020) with 95% confidence ellipses. (c) Topography, active faults, and earthquakes of the Kepingtag fold-and-thrust belt. Focal mechanisms are from teleseismic body-waveform modelling studies or the Global Centroid Moment Tensor (CGMT) catalog (see Table 1 for details). They are plotted at our relocated epicenters, coloured by year and scaled by magnitude. The black dashed box shows the location of Figure 2.

by shallow folding and blind faulting without accompanying surface rupture. There are many other examples of large earthquakes that ruptured faults that were not previously mapped, and where historical and instrumental records were too short to have revealed the associated seismic hazard beforehand. Furthermore, fold-and-thrust belts contain a wide range of fault structures including décollements and ramp-and-flat thrusts, and it is often not clear which of these host large earthquakes and which creep aseismically (e.g., Copley, 2014; Ainscoe et al., 2017; Mallick et al., 2021). It is also important to consider how subsurface structure and stratigraphy may influence rupture extents, and thus potential earthquake magnitudes (e.g., Elliott et al., 2011; Nissen et al., 2011).

On January 19 2020 at 13:27:56 UTC, a $M_w$ 6.0 earthquake struck near Jiashi in the western Kepingtag belt ($\sim$39.83°N, 77.21°E) (Fig. 1), causing intense ground shaking and damage to hundreds of buildings. A regional seismic network recorded 1,639 aftershocks as of February 11 2020 (Ran et al., 2020), with the largest ($M_b$ 5.1) occurring $\sim$1 hour after the mainshock. This sequence provides an opportunity to investigate patterns of seismicity and deformation in this region. Routine teleseismic moment tensor solutions for the mainshock from the U.S. Geological Survey (USGS) and the Global Centroid Moment Tensor project (GCMT) implicate thrust or reverse faulting, but exhibit discrepancies of tens of degrees in strike, dip, and rake and of several kilometers in centroid depth and location. This makes it difficult to associate the earthquake with specific faulting or characterize its tectonic implications without further investigation (Engdahl et al., 2006; Weston et al., 2011; Wimpenny & Scott Watson, 2020).

Interferometric Synthetic Aperture Radar (InSAR) observations and modelling can provide more precise constraints on fault geometries and depth extents of large, shallow continental earthquakes (e.g., Elliott et al., 2016). Furthermore, growing compilations of seismic phase arrival times can help relocate earthquake hypocenters more accurately which, in conjunction with InSAR slip models, can provide additional information on rupture directivity (e.g., Pousse-Beltran et al., 2020). In this paper, we map the surface deformation of the 2020 Jiashi earthquake using the Sentinel-1 InSAR imagery and characterize its subsurface fault geometry and slip distribution using elastic dislocation modelling. We provide an independent check on its mechanism and centroid depth using teleseismic body waveform modelling and pinpoint its hypocenter using a calibrated, multi-event relocation. We relate some striking features of the surface deformation and slip model to the subsurface structure of the Kepingtag belt. Our multi-event relocation also allows us to re-assess earlier instrumental earthquakes in this region. These new results are used to reevaluate the active tectonics and seismic hazard of the Kepingtag belt.

## 2 TECTONIC SETTING

The Tian Shan in Central Asia originally formed in the Paleozoic, and most of the present topography of the mountain ranges resulted from Cenozoic reactivation as a result of the India-Eurasia collision (Windley et al., 1990; Hendrix et al., 1992; Avouac & Tapponnier, 1993; Burchfiel et al., 1999). Over time, the deformation has propagated outward into the Tarim and Junggar basins, where along certain parts of the Tian Shan margins, intense folding and faulting have created sets of narrow ridges. The Kepingtag fold-and-thrust belt, located along the arid southern margin of the Chinese Tian Shan, offers one of the clearest examples of this basinward migration of active deformation (Fig. 1b).

### 2.1 Geology of the Kepingtag belt

About 200 km long by 50 km wide and trending WSW–ENE, the Kepingtag belt consists of fault-related folds associated with a series of south-verging, imbricated thrust stacks (Allen et al., 1999). Folded strata are composed of Cambrian–Ordovician Qiulitag group limestones, Middle Ordovician Saergan group limestone and dolomite, Silurian Kepingtag group sandstone, Devonian sandstone, Carboniferous Kangkelin group sandstone, lower Permian limestone, and Paleogene–Neogene Wuqia group sandstone and conglomerate (Chen et al., 2006; Yang et al., 2010). The thickness of the upper Paleozoic strata in the Kepingtag belt increases from about 2 km in the south to greater than 4 km in the north (Yin et al., 1998). There is a major angular unconformity between the Paleozoic strata and the Cenozoic foreland basin deposits, with the near absence of Mesozoic sedimentary rocks implying significant Paleozoic crustal shortening.

The thick Paleozoic sequence of mainly Upper Cambrian to Permian strata is exposed in

**Table 1.** Earthquake source parameters in the Kepingtag belt and its foreland. Relocated hypocenters are from this study. The focal depth (FD) is followed by a superscript letter describing how it was calibrated: $d$ = teleseismic depth phases, $l$ = local-distance readings, $n$ = near-source station readings, and $c$ = cluster default depths. Focal mechanisms are taken from *(1)* Fan et al. (1994), *(2)* Sloan et al. (2011), *(3)* Ghose et al. (1998), *(4)* the Global Centroid Moment Tensor (GCMT) catalogue, and *(5)* this study. The centroid depth (CD) is also given a superscript letter that describes whether it was obtained by modelling ($t$) teleseismic body-waveforms, ($d$) teleseismic depth phases, ($r$) regional waveforms, or ($i$) = InSAR surface displacements. Where only a less reliable GCMT centroid depth is available, we mark the solution with an asterisk.

| | | *Relocated hypocenter* | | | *Focal mechanism* | | | | | |
|---|---|---|---|---|---|---|---|---|---|---|
| Date | Time | Long. | Lat. | FD (km) | CD (km) | Strike | Dip | Rake | $M_w$ | Ref. |
| 1977.12.18 | 16:47 | 77.4065 | 39.9236 | $22^d$ | $7^t$ | 74 | 51 | 79 | 5.8 | *1* |
| 1986.04.25 | 16:12 | 77.3404 | 40.1340 | $13^d$ | 15* | 283 | 60 | 125 | 5.4 | *4* |
| 1996.03.19 | 15:00 | 76.7353 | 40.0810 | $13^l$ | $34^t$ | 234 | 16 | 87 | 6.0 | *2* |
| 1996.03.20 | 00:14 | 76.8644 | 40.0562 | $17^l$ | $6^r$ | 268 | 20 | 76 | 4.5 | *3* |
| 1996.03.22 | 08:26 | 76.7983 | 40.0816 | $15^l$ | $6^r$ | 260 | 18 | 78 | 5.2 | *3* |
| 1996.04.02 | 02:28 | 77.5587 | 40.2328 | $10^l$ | $16^r$ | 242 | 59 | 128 | 4.1 | *3* |
| 1997.01.21 | 01:48 | 77.2050 | 39.6475 | $11^l$ | $12^t$ | 317 | 85 | 177 | 5.4 | *2* |
| 1997.01.29 | 08:20 | 76.9678 | 39.5923 | $12^l$ | 33* | 04 | 83 | 132 | 5.2 | *4* |
| 1997.03.01 | 06:04 | 76.9532 | 39.5288 | $14^l$ | $14^d$ | 180 | 80 | −173 | 5.6 | *2,4* |
| 1997.04.05 | 23:36 | 76.9622 | 39.5832 | $12^l$ | $18^t$ | 177 | 64 | −139 | 5.4 | *2* |
| 1997.04.06 | 04:36 | 77.0809 | 39.5694 | $12^l$ | $17^t$ | 246 | 41 | −74 | 5.8 | *2* |
| 1997.04.06 | 12:58 | 77.0324 | 39.6105 | $17^l$ | $13^t$ | 210 | 38 | −74 | 5.1 | *2* |
| 1997.04.11 | 05:34 | 77.0326 | 39.6023 | $15^n$ | $20^t$ | 226 | 42 | −79 | 6.0 | *2* |
| 1997.04.12 | 21:09 | 77.0039 | 39.5334 | $14^n$ | $16^t$ | 239 | 27 | −74 | 5.1 | *2* |
| 1997.04.15 | 18:19 | 77.0506 | 39.6461 | $14^n$ | $18^t$ | 177 | 64 | −139 | 5.7 | *2* |
| 1997.06.24 | 09:24 | 76.9562 | 39.5877 | $16^n$ | 34* | 345 | 72 | −167 | 5.1 | *4* |
| 1997.10.17 | 17:35 | 77.0875 | 39.5686 | $25^d$ | 33* | 177 | 64 | −139 | 5.3 | *4* |
| 1998.03.19 | 13:51 | 76.8048 | 40.1732 | $15^l$ | $15^d$ | 243 | 5 | 79 | 5.6 | *2,4* |
| 1998.08.02 | 04:40 | 77.0897 | 39.6817 | $10^d$ | $15^t$ | 173 | 40 | −140 | 5.5 | *2* |
| 1998.08.03 | 15:15 | 77.0905 | 39.6527 | $15^l$ | $29^r$ | 253 | 10 | 129 | 4.6 | *2* |
| 1998.08.27 | 09:03 | 77.4554 | 39.6437 | $16^l$ | $15^t$ | 57 | 80 | 1 | 6.3 | *2* |
| 1998.09.03 | 06:43 | 77.4162 | 39.6528 | $25^d$ | $10^r$ | 179 | 59 | 178 | 4.8 | *2* |
| 1998.10.31 | 16:09 | 77.2469 | 39.6081 | $19^l$ | $14^r$ | 152 | 74 | −164 | 4.6 | *2* |
| 2003.01.04 | 11:07 | 77.0350 | 39.6389 | $14^l$ | 33* | 245 | 73 | −20 | 5.2 | *4* |
| 2003.02.24 | 02:03 | 77.3157 | 39.5852 | $19^l$ | $5^t$ | 280 | 17 | 115 | 6.2 | *2* |
| 2003.02.24 | 21:18 | 77.2653 | 39.5663 | $12^l$ | 15* | 289 | 33 | 126 | 5.2 | *4* |
| 2003.02.25 | 03:52 | 77.4717 | 39.5385 | $8^l$ | 15* | 239 | 33 | 62 | 5.3 | *4* |
| 2003.03.12 | 04:47 | 77.5273 | 39.4969 | $8^l$ | $7^d$ | 245 | 33 | 73 | 5.7 | *2,4* |
| 2003.03.15 | 22:59 | 77.3459 | 39.5733 | $9^l$ | 15* | 330 | 57 | 178 | 5.0 | *4* |
| 2003.03.30 | 23:15 | 77.4315 | 39.5462 | $17^l$ | $10^t$ | 287 | 27 | 117 | 5.2 | *2* |
| 2003.05.04 | 15:44 | 77.2305 | 39.4369 | $9^l$ | 15* | 308 | 53 | 179 | 5.8 | *4* |
| 2003.06.04 | 16:28 | 77.6458 | 39.4665 | $10^l$ | $10^d$ | 274 | 54 | 92 | 5.2 | *2,4* |
| 2003.09.26 | 23:35 | 77.1664 | 40.2902 | $30^d$ | 15* | 290 | 13 | 58 | 5.3 | *4* |
| 2004.10.07 | 16:14 | 77.4633 | 40.2740 | $12^l$ | 17* | 245 | 14 | 72 | 4.8 | *4* |
| 2005.03.24 | 07:37 | 77.7478 | 39.9288 | $11^d$ | 30* | 187 | 35 | 32 | 4.8 | *4* |
| 2006.06.08 | 11:34 | 77.6951 | 40.4025 | $6^d$ | 30* | 290 | 35 | 113 | 4.8 | *4* |
| 2006.09.06 | 07:51 | 76.9389 | 40.3257 | $15^l$ | 32* | 258 | 37 | 91 | 4.7 | *4* |
| 2009.04.22 | 09:26 | 77.2583 | 40.1229 | $11^d$ | 16* | 264 | 50 | 124 | 5.0 | *4* |
| 2009.10.16 | 02:56 | 76.9545 | 39.9836 | $15^d$ | 19* | 284 | 32 | 116 | 5.0 | *4* |
| 2011.08.11 | 10:06 | 77.1232 | 39.9575 | $19^d$ | 12* | 272 | 42 | 109 | 5.6 | *4* |
| 2012.08.11 | 09:34 | 78.2335 | 40.0027 | $15^d$ | 12* | 255 | 43 | 84 | 5.3 | *4* |
| 2013.03.11 | 03:01 | 77.4916 | 40.1729 | $9^d$ | 12* | 210 | 11 | 50 | 5.2 | *4* |
| 2015.01.10 | 06:50 | 77.2838 | 40.1469 | $14^c$ | 15* | 227 | 17 | 57 | 5.1 | *4* |
| 2016.07.09 | 16:36 | 78.0578 | 40.0128 | $14^c$ | 12* | 240 | 32 | 53 | 4.8 | *4* |
| 2018.04.12 | 10:41 | 77.4068 | 40.4104 | $17^l$ | 22* | 231 | 36 | 50 | 4.9 | *4* |
| 2018.09.03 | 21:52 | 76.9341 | 39.5211 | $14^c$ | 15* | 317 | 89 | 178 | 5.5 | *4* |
| 2018.11.03 | 21:36 | 77.6323 | 40.2120 | $14^c$ | 12* | 225 | 12 | 63 | 4.9 | *4* |
| 2019.01.06 | 16:22 | 77.6093 | 39.9331 | $6^d$ | 12* | 238 | 50 | 79 | 4.9 | *4* |
| 2020.01.17 | 16:05 | 77.1167 | 39.8682 | $12^d$ | 21* | 261 | 86 | −178 | 5.3 | *4* |
| 2020.01.19 | 13:27 | 77.1161 | 39.8944 | $11^d$ | $7^i$ | 279 | 7 | 115 | 6.0 | *5* |
| 2020.01.19 | 14:23 | 77.4089 | 39.9236 | $14^c$ | 18* | 268 | 22 | 95 | 5.1 | *4* |
| 2020.02.21 | 15:39 | 77.4059 | 39.9232 | $14^c$ | 14* | 287 | 46 | 143 | 4.8 | *4* |

a series of parallel anticlines (Xinjiang Bureau of Geology and Mineral Resources, 1993). The hanging wall cut-offs of the imbricate thrusts have been eroded away. This thrust system is interpreted as thin-skinned, with fault-propagation folds detached in Upper Cambrian limestones along a décollement at $\sim$6–10 km depth according to seismic reflection profiles and balanced geological cross-sections (Allen et al., 1999; Yin et al., 1998; Nishidai & Berry, 1990; Yang et al., 2010). The left-lateral Piqiang fault (Fig. 1) has developed perpendicular to the Kepingtag belt, dividing it into two (western and eastern) segments. Interpretations of satellite imagery and balanced cross-sections suggest that the thin-skinned imbricate thrusting and folding has accommodated crustal shortening strains of 20–28$\%$ between the main Tian Shan and Tarim block, equivalent to $\sim$35 km across the western segment and $\sim$22 km across the eastern segment (Allen et al., 1999; Yin et al., 1998).

## 2.2 Seismicity of the Kepingtag belt and its foreland

Active crustal shortening and thickening of the southern Tian Shan is manifest in frequent reverse faulting earthquakes that cluster around the margins of the high topography with nodal planes oriented approximately parallel to the range (Ghose et al., 1998; Xu et al., 2006; Sloan et al., 2011). The Kepingtag belt and its adjacent foreland are amongst the most seismically-active parts of the Tian Shan, with thirty-six earthquakes of $M_w$ 5.0–6.3 since the late 1970s (Fig. 1b and Table 1). The 1902 $M_w$ 7.7 Atushi (Kashgar) earthquake, located $\sim$150 km west of our study area, hints that much larger earthquakes may be possible (Kulikova & Krüger, 2017). Within the Kepingtag belt, instrumental seismicity is concentrated west of the Piqiang fault and the available focal mechanisms indicate a predominance of thrust and reverse faulting. Assuming that northward-dipping nodal planes represent faulting, dip angles range from $\sim$5°–60° with an average of around 30°. Only a few of these events have reliable centroid depths from detailed waveform modelling, mostly in the range 6–16 km, consistent with faulting within the lower sedimentary cover and the underlying basement (Fan et al., 1994; Ghose et al., 1998; Sloan et al., 2011). Sloan et al. (2011) placed a single outlier event at 34 km depth, within the middle-to-lower crust, but noted that its relatively complex waveforms could potentially be explained by a compound (multi-event) source mechanism at a much shallower depth.

Between 1997 and 1998, thirteen earthquakes of $M_w$ 5.0–6.3 struck the foreland south of the Kepingtag belt. These included the destructive January-October 1997 Jiashi earthquake swarm , which caused 21 fatalities (Zhang et al., 1999). This sequence involved a mix of strike-slip and normal faulting with well-resolved centroid depths of $\sim$12–20 km (Sloan et al., 2011), as well as some smaller, deeper earthquakes located by a temporary regional network but without reliable focal mechanisms (Xu et al., 2006). The mechanisms and depths are challenging to interpret but may reflect flexural rebound of the Tarim basin under loading from the Tian Shan (Sloan et al., 2011). On February 24 2003, the $M_w$ 6.2 Bachu-Jiashi earthquake struck the same area, resulting in 261 reported fatalities. In contrast with the 1997 swarm, the 2003 earthquake involved northward-dipping thrust faulting with a much shallower centroid depth of $\sim$5–7 km, interpreted to represent southward propagation of the Kepingtag belt into the Tarim basin (Sloan et al., 2011). It also produced an abundant aftershock sequence that was apparently concentrated in the middle crust between $\sim$15–25 km (Huang et al., 2006). Following the 2003 Bachu-Jiashi sequence, the Kepingtag belt and its foreland entered a relatively quiescent period of seismic activity, with no earthquake of magnitude 6 or above until the January 19 2020 event.

The 2020 Jiashi sequence occurred within the frontal, western Kepingtag belt. The sequence was recorded by thirteen permanent stations at $\sim$30–170 km distance and by two local stations $\sim$20 km SW and NW of the mainshock epicenter, which were deployed by the Xinjiang Earthquake Administration 4 and 18 hours after the mainshock, respectively. These regional recordings have been used as the basis of three previous seismological studies of the sequence, summarized below (Ran et al., 2020; Yao et al., 2021a; He et al., 2021). The $M_w$ 6.0 mainshock was preceded by two days of foreshock activity involving $\sim$N–S-oriented left-lateral strike-slip faulting. The mainshock itself ruptured an $\sim$E–W-oriented thrust or reverse fault, though there is disagreement amongst available seismological and geodetic models on its geometry and depth, which will be discussed further in light of our own results in Section 4. The mainshock was followed by an energetic aftershock sequence of several hundred events that lasted at least three months. Double-difference relocated seismicity forms a ‘T’ shaped pattern in map view, with the mainshock located at the bottom of the ‘T’ and aftershocks extending $\sim$20 km northward to the junction of the ‘T’, and from there, $\sim$20 km east and west for a total length of $\sim$40 km, with the greatest concentration of events along the western branch (Ran et al., 2020; Yao et al., 2021a; He et al., 2021). The double differencing also shows that the aftershocks are concentrated at depths of 10–20 km (Figs. S12 and S13).

## 3 METHODS

### 3.1 InSAR measurements and modelling

We used InSAR to measure surface deformation in the January 19 2020 earthquake, and elastic dislocation modelling to estimate the fault geometry and slip distribution. The raw data are from the European Space Agency’s C-band Sentinel-1A satellite, with wavelength $\sim$5.6 cm. Two ascending tracks (056A and 129A) and one descending track (034D) capture the Jiashi mainshock. Three, 12 day coseismic interferograms (January 11–23, January 16–28 and January 10-22 2020) were processed using GAMMA software (Werner et al., 2000) and multi-looked to four looks in range and twenty in azimuth to achieve a $\sim$30 m $\times$ 30 m pixel resolution. The topographic phase contribution was removed using the 30 m-resolution Shuttle Radar Topographic Mission Digital Elevation Model, which was also used to geocode the interferograms. The two ascending-track interferograms were unwrapped using the branch-cut algorithm (Goldstein et al., 1988) while the noisier, descending-track interferogram was unwrapped using the Minimum Cost Flow algorithm.

The interferograms exhibit excellent coherence, reflecting the dry desert conditions and sparse vegetation of the southwestern Tian Shan. Coseismic surface deformation is easily distinguished in all three interferograms as a double fringe ellipse elongated in an E-W orientation (Fig. 2a, d, g). The southern lobe is focused on the Kepingtag anticline and exhibits up to $\sim$7.5 cm of line-of-sight (LOS) displacement toward the satellite, and the northern lobe is centered along the Aozitag anticline and contains up to $\sim$5 cm of displacement away from the satellite (Fig. 7a–c). The similarity of the fringe patterns in ascending and descending interferograms implies that the largest contribution to the observed LOS deformation is from uplift/subsidence rather than E/W lateral displacement, consistent with predominantly dip-slip faulting. We also observe some localized deformation along the southern Kepingtag rangefront its proximal foreland basin. The short wavelengths, and absence of shallow aftershocks in this area, hints that this deformation is caused by secondary effects such as landsliding or liquefaction, and/or subsidence from agricultural activity (e.g. through aquifer drawdown).

After downsampling the LOS displacements using a quadtree algorithm to concentrate sampling in regions with high phase variance (Jónsson et al., 2002), we employed a routine, two-step inversion strategy to estimate the causative fault parameters (e.g. Wright et al., 1999, 2004; Funning et al., 2005; Elliott et al., 2013, 2015; Ainscoe et al., 2017; Pousse-Beltran et al., 2020). In the first step, we inverted the downsampled data to solve for the optimal strike, dip, rake, slip, length, and top and bottom depths of a rectangular, uniform slip model fault plane buried within an elastic half space; we also jointly solved for nuisance parameters (a static shift and linear ramp in LOS displacement for each interferogram to account for their different unwrapping reference points, satellite orbital errors, and long-wavelength lateral variations in tropospheric delay) and weighted the single descending interferogram equal to the two ascending interferograms. We used Okada's expressions (Okada, 1985) to relate model fault slip to deformation of the free surface, applied a non-linear, downhill Powell's algorithm (Press et al., 1992) to obtain the minimum misfit parameters, and ran 500 Monte Carlo restarts with random starting parameters to sample the parameter space fully and avoid local minima (Wright et al., 1999). Without firm constraints on how rheological properties vary with depth locally, we assumed an elastic half space with standard Lamé parameters ($\lambda$ and $\mu$) of 3.2 $\times$ $10^{10}$ Pa. We anticipate that this assumption only moderately impacts the retrieved fault parameters; for example, tests of layered and half-space elastic structures for a similar magnitude, buried earthquake in Tibet showed differences of $<1^\circ$ in fault strike and dip, $\sim6^\circ$ in rake, 0.2–0.5 km in fault length, top and bottom depths, and center coordinates, and 5–8% in slip and moment (Bie et al., 2014). We also assumed a flat free surface, which is appropriate given the limited ($<1$ km) relief across the study area and is not expected to impact the retrieved fault parameters significantly (Li & Barnhart, 2020). Finding a trade-off between slip and fault width — which is common for buried earthquakes (e.g. Funning et al., 2005; Elliott et al.,

2013) — we obtained the initial fault geometry by fixing slip to 1.0 m. Inversions performed with 0.5 m, 1.5 m and 2.0 m show that this choice makes no significant difference to the resulting fault geometry, with variations of $<1^\circ$ in the resulting model fault strike, dip and rake, and $<0.5$ km in fault length and fault center point latitude, longitude and depth (Table S1).

In the second step, we estimated the slip distribution by extending the uniform slip model fault plane along strike and up- and down-dip, dividing it into 1 km $\times$ 1 km sub-fault patches, and solving for slip on each patch (with rake fixed to the uniform slip solution) using a Laplacian operator to vary smoothing (Wright et al., 2004; Funning et al., 2005) and a non-negative least squares algorithm to ensure positive slip (Bro & De Jong, 1997). We solved for the best-fitting slip model and nuiscance parameters, m, using the equation,

$$\begin{pmatrix} \mathbf{G} \\ \kappa\nabla^2 \end{pmatrix} \mathbf{m} = \begin{pmatrix} \mathbf{d} \\ 0 \end{pmatrix}$$

where G is the matrix of Green's functions (LOS displacements calculated at downsampled data locations using the formulation of Okada (1985) for 1 m of slip on each fault patch), $\nabla^2$ is the finite difference approximation of the Laplacian operator which acts to smooth the distribution of slip, $\kappa$ is a scalar smoothing factor which determines the relative importance of the smoothing operator, and d contains the downsampled LOS displacements. We settled upon a preferred smoothing factor that represents a compromise between decreasing the fault slip roughness to prevent unrealistic, oscillating slip distributions, while minimizing the resulting increase in misfit (Wright et al., 2004). The resulting model still included a few outlier slip patches that lay several kilometers up-dip from the main slip distribution, which we consider spurious and exclude from our final, reported results. These are tabulated in Supplementary Table S3, and were used to generate the forward model and residual interferograms shown in Fig. 2.

Given the structural complexity of the Kepingtag belt, we also investigated whether the Jiashi earthquake may have involved non-planar rupture geometries by inverting the InSAR displacements for two uniform slip model fault planes (e.g., Pousse-Beltran et al., 2020). We explored a range of listric and anti-listric configurations by matching the top depth of a deeper model fault to the bottom depth of a shallower model fault, and allowing their dips to vary independently and up to angles as steep as 32.5°. Though the large number of free parameters in these two-fault models make it challenging to explore fully this parameter space, none of the two-fault configurations that we tested produced a realistic geometry that improved upon the misfit of the simple, single-fault model. This leads us to favour involvement of a single, planar fault.

We did not have access to GNSS data that could potentially constrain our slip model further, though we know of six stations within $\sim$100 km of the mainshock that may have exhibited coseismic offsets (Figure 1; Wang et al. (2020)). Instead, we provide a table of displacements at these sites predicted by our preferred, InSAR-derived distributed slip model (Supplementary Table S6). These could be used for comparison by any future GNSS study of the Jiashi sequence.

## 3.2 Calibrated hypocenter relocations

We relocated hypocenters of the January 19 2020 Jiashi mainshock and its principal foreshock ($m_b$ 4.3) and two largest aftershocks ($m_b$ 5.1 and 5.0) using teleseismic, regional and local seismic phase arrival times. Thirty-seven well-recorded background events starting from 2003 were also relocated, providing the repeated phase observations at common stations and the improved azimuthal coverage at local distances needed to calibrate the cluster, by which we mean minimizing hypocentral biases from unknown Earth structure and reliably quantifying their uncertainties (Bergman et al., submitted). We adopt the Hypocentroidal Decomposition relocation approach of Jordan & Sverdrup (1981) which separates the relocation into two distinct inverse problems, each reliant on customized phase arrival time data. We solve first for the relative locations of each hypocenter with respect to the reference hypocentroid (defined as the arithmetic mean of all individual event hypocenters within the cluster) using arrival data at all distances, allowing us to capitalize upon the abundance of teleseismic phase picks available for larger events in the cluster. We then solve for the absolute location of the hypocentroid using only locally recorded, direct *Pg* and *Sg* phases, which are impacted least by unknown Earth structure. This enables us to update the absolute hypocenter coordinates of every event in the cluster. In other, comparably instrumented regions, direct calibrations (ones that utilize local seismic data to solve for the hypocentroid) have resolved epicenters to within $\sim$1–2 km (at 90% confidence) and focal depths to within $\sim$5 km

(Karasözen et al., 2019), improving substantially on the uncertainties of routine catalogs such as the USGS and GCMT (Engdahl et al., 2006). Juxtaposing calibrated epicenters with InSAR-derived slip models can distinguish bilateral from unilateral rupture propagation (e.g., Gaudreau et al., 2019; Pousse-Beltran et al., 2020) and help resolve ambiguities in subsurface fault geometry, which are otherwise commonplace for buried earthquakes (e.g., Roustaei et al., 2010; Copley et al., 2015; Elliott et al., 2015; Karasözen et al., 2018).

The cluster was relocated and calibrated in the *Mloc* program (Walker et al., 2011; Karasözen et al., 2016; Bergman et al., submitted) using a customized travel-time model (Table S2) comprising a 3-layered crust of thickness 50 km — consistent with several previous estimates of regional Moho depths (Gao et al. (2013) and references therein) — over the upper mantle portion of the global 1D model ak135 (Kennett et al., 1995). For the best-recorded events, we estimated focal depths using local arrival times; for others, we relied upon teleseismic depth phases or simply fixed the focal depth to a representative cluster default of 14 km (Fig. S1). We estimated the hypocentroid using epicentral distances of up to 2°, for which there is excellent azimuthal coverage (Fig. S2); average residual travel times for phases used in this direct calibration are 0.0 sec for *Pg* and 0.1 sec for *Sg* (Fig. S3). Observed phase arrivals and theoretical travel times for distances of up to 4°, 15° (for shear phases), and 30° are shown in Supplementary Figs. S4–S6. The final relocated hypocenters, including epicentral uncertainties at 90% confidence, are provided in Supplementary Table S3.

Our results were then combined with an earlier *Mloc* relocation cluster focused on the 1997 Jiashi earthquake swarm and the 2003 Bachu-Jiashi earthquake in the foreland south of the Kepingtag belt (Bergman et al., submitted). The earlier cluster adopted the same relocation procedure and the same regional velocity structure for the crust and upper mantle as this study. The earlier cluster is available through the Global Catalog of Calibrated Earthquake Locations (GCCEL) database (Bergman et al., submitted) and figures in the main paper incorporate both relocated datasets.

### 3.3 Teleseismic body waveform inversion

Finally, we used teleseismic body waveform modelling to provide additional constraints on the mainshock source depth and mechanism, complementing those from InSAR analysis. Modelling of both seismological and geodetic data is important when there are disagreements in the depth of faulting, as is the case for the Jiashi earthquake (see Section 4). Centroid depths obtained from waveform modelling can also help clarify whether fault slip resolved by InSAR models occurred coseismically or through afterslip (Nissen et al., 2014).

We followed the approach of Heimann et al. (2018), and inverted vertical and transverse component data from stations between 3,300 km and 9,900 km from the reported earthquake location (Supplementary Fig. S7). Waveforms were filtered between 0.01 and 1 Hz, and we used a window starting 15 seconds before, and ending 25 seconds after, the principle phase (*P* for vertical component waveforms, *S* for transverse component waveforms). Synthetic seismograms were generated using the velocity structure determined in our calibrated relocation (Section 3.2 and Supplementary Table S2). The source-time function is constrained to be a variable-duration half-sinusoid — appropriate for an earthquake of this size, and for the frequencies used in our inversions. Observed data and synthetics were aligned using cross correlation. The Bayesian approach outlined in Heimann et al. (2018) allows for the full sampling of the parameter space available in source depth, latitude, longitude, magnitude, and mechanism (Supplementary Figures S8–S9). Misfits between observed and synthetic waveforms are plotted in Supplementary Figures S10–S11.

## 4 RESULTS

Our best-fitting InSAR uniform slip model fault strikes 279°, dips 7° N, has a slight right-lateral component (rake 115°), and is $\sim$22 km long by $\sim$2 km wide, centered at 7 km depth (Table 2). To further test model sensitivity to centroid depth, we ran the inversion by prescribing different (fixed) top and bottom depths while allowing other parameters to vary freely. We also undertook similar tests of model sensitivity to dipping angle and fault width (aspect ratio). There is a fairly steep increase in misfit at fault center depths shallower or deeper than the minimum misfit value of 7 km (Fig. 3). For the equivalent dip sensitivity test, we find low misfits for dip angles of 5–10°, but abrupt increases in root mean square error outside of this range (Fig. 4a). For the fault width test, we find that extending the fault plane up- and down-dip leads to larger misfits, particularly when the aspect ratio (length to width) is forced from the minimum misfit value of $\sim$12 to below $\sim$6. This shows that the highly-elongated model rupture area is real (Fig. 4b).

Compared to the uniform slip model, our preferred distributed slip model is longer at $\sim$37 km and wider at $\sim$9 km, but remains centered at $\sim$7 km depth (Fig. 5). The slip distribution is characteristically narrow, with an aspect ratio (length to width) of around 4. The peak slip is $\sim$0.5 m and the model moment is $\sim 1.75 \times 10^{18}$ N. The resultant forward model interferogram matches the observed surface deformation closely, with less than one residual fringe and a root mean square residual of $\sim$0.25 cm (Fig. 2c, f, i), which is substantially lower than that of the uniform slip model ($\sim$0.35 cm). The close agreement between observed and forward model coseismic fringe patterns implies that the more localized deformation along the Kepingtag rangefront had negligible impact on our modelling.

Our InSAR model fault plane is 10° different in strike and 17° different in rake from the N-dipping nodal plane of the USGS body-wave moment tensor, and there are even larger discrepancies in strike and rake with the USGS W-Phase and GCMT solutions (Table 2). However, of the four mechanisms the InSAR model strike is most closely aligned with $\sim$E–W trends in local faulting, geological structure and topography. Furthermore, the shallow-dipping nodal planes of the USGS and GCMT models are poorly constrained by teleseismic data and liable to be affected by a strong trade-off between strike and rake (e.g. Beckers & Lay, 1995). Our distributed slip model is 17–26% larger in moment than the three available seismological catalogue solutions.

Four other InSAR-derived fault models are also available for comparison (Table 2). Our model is closest to that of He et al. (2021) and to the single fault solution of Yu et al. (2020); the three models agree to within 4° in strike and dip, to within 6° in rake, and to within 1 km in centroid depth. Yu et al.'s preferred, two-fault model is strongly listric, with slip apportioned between a deep, gentle (2°) décollement and a much steeper (52°) ramp. However, we prefer the single-fault solution, as the two-fault models we tested using different configurations of listric and antilistric faults could not yield smaller misfits. Our model is $\sim$2 km deeper and significantly shorter and narrower than a uniform slip model by Yao et al. (2021b). However, they do not provide model or residual interferograms, so there is no easy way to assess the accuracy of their model.

Our relocated mainshock hypocenter lies beneath the northern limb of Kepingtag anticline, which is located $\sim$6.6 km NNW from one inferred by Ran et al. (2020) using local data. However, our epicenter is somewhat closer to the InSAR-derived slip distribution patch, lying at its far western end. Both our model and Ran et al. (2020)'s show that the Jiashi earthquake is strongly unilateral, rupturing from west to east (Supplementary Fig. S12). Our relocated epicenter of the January 17, 2020 $m_b$ 4.3 foreshock lies $\sim$3 km SE from the mainshock, and the two largest aftershocks ($m_b$ 5.1 and 5.0) lie near the eastern end of the mainshock model slip patch (Fig. 1c).

We show the results of our seismological inversions in Fig. 6 and synthetic waveforms for all stations used in the inversion in Supplementary Fig. S10–S11. A probability density function (PDF) of centroid depth results from an inversion with all parameters free shows both the mean and the best-fit solution at just under 10 km (Fig. 6a). Using teleseismic data offers good constraints on the mechanism only near the center of the focal sphere, where the pierce-points of teleseismic body waves cluster. As such, the mechanism, and particularly the shallowly dipping nodal plane are poorly constrained (inset mechanism, Fig. 6a). Consequently, we repeated the inversion using double couple nodal planes fixed to match the InSAR-determined fault plane (Fig. 6b). This pushes the PDF slightly deeper, with a mean depth at 11 km, but with a best-fit solution still at 10 km, and makes only a marginal difference to the overall misfit values. We also show the PDF for the seismologically-determined magnitude in Fig. 6c, which matches well with the inferred magnitude of the geodetic signal. The model source time function duration of 8–10 seconds is rather long for a $M_w$ 6.0 thrust earthquake (e.g. Bayasgalan et al., 2005; Nissen et al., 2007; Elliott et al., 2015) and supports our inference of unilateral rupture of a $\sim$22–37 km fault assuming typical propagation speeds of 1.5–4 km/s (Chounet et al., 2018).

In order to illustrate the constraints that the teleseismic data offer on the centroid depth, we show a set of six example waveforms (three vertical components, three transverse component) and best-fit synthetics calculated using three fixed centroid depths in Fig. 6d. The middle row shows waveforms calculated at 10 km centroid depth, which is the best fit seismological solution, while

**Table 2.** Source parameters of the 2020 Jiashi mainshock inferred from our model and other sources. The longitude and latitude listed for our InSAR-derived models (first two rows) represent the surface projection of the model slip plane; our relocated epicenter is 77.117° E and 39.894° N. The other InSAR studies parameterize the fault location differently. Depths are given as the top, middle (or centroid) and bottom depths of the slip plane in that order. L and W are length and width, respectively. Yu et al. (2020) prefer their listric, two fault model with a deeper, flatter segment fixed at 2° dip and a shallower, steeper ramp at 52°. Yao et al. (2021b) used uniform slip of 0.32 m in their InSAR-derived model, which may account for their much larger model fault plane.

| Source | Long. | Lat. | Strike | Dip | Rake | Depth (km) | L/W (km) | Moment (Nm) | $M_w$ |
|---|---|---|---|---|---|---|---|---|---|
| This study, uniform slip | 77.279° | 39.902° | 279° | 7° | 115° | 7.0/7.1/7.2 | 22/2 | $1.31 \times 10^{18}$ | 6.0 |
| This study, distributed slip | 77.165° | 39.416° | 279° | 7° | 115° | 6.3/7.0/7.6 | 37/9 | $1.75\times 10^{18}$ | 6.0 |
| USGS body-wave | 77.11° | 39.84° | 262° | 9° | 105° | –/4/– | – | $1.493 \times 10^{18}$ | 6.1 |
| USGS $W$-phase | 77.11° | 39.84° | 221° | 20° | 72° | –/19.5/– | – | $1.387 \times 10^{18}$ | 6.0 |
| CGMT | 77.19° | 39.80° | 196° | 38° | 31° | –/11/– | – | $1.39 \times 10^{18}$ | 6.0 |
| Yu et al. (2020), 1 fault | 77.30° | 39.91° | 275° | 9° | 111° | –/6.3/– | – | – | 6.1 |
| Yu et al. (2020), 2 faults | 77.30° | 39.90° | 275° | 2°/52° | 111° | –/4.15/– | – | – | 6.1 |
| Yao et al. (2020) | 77.86° | 39.31° | 269° | 20° | 92° | 4/5/6 | 58/30 | $2.29 \times 10^{18}$ | 6.2 |
| He et al. (2021) | 77.45° | 39.79° | 276° | 10.2° | 109° | 5/7.3/9.6 | 50/26 | $- \times 10^{18}$ | 6.08 |

the upper row shows waveforms with the depth fixed to match the geodetic results at 7 km, and the lower row shows waveforms with the depth fixed to match the centre of the regionally-determine aftershock distribution at 15 km. We discuss these waveform misfits further in the following section.

# 5 DISCUSSION

## 5.1 Depth discrepancy between the 2020 Jiashi mainshock and its aftershocks

Our InSAR-derived model suggests that the Jiashi mainshock ruptured along the décollement at the base of the sedimentary cover, with a centroid depth of ∼7 km. From the high-quality locally-recorded and double-difference relocated aftershock data, aftershocks cluster along E–W and NNW–SSE trends, with the former matching the ∼40 km length and orientation of our slip model (Supplementary Figs. S12 and S13) (Ran et al., 2020; Yao et al., 2021a; He et al., 2021). However, locally-recorded aftershocks concentrate at 10–20 km depth, well below the depth of

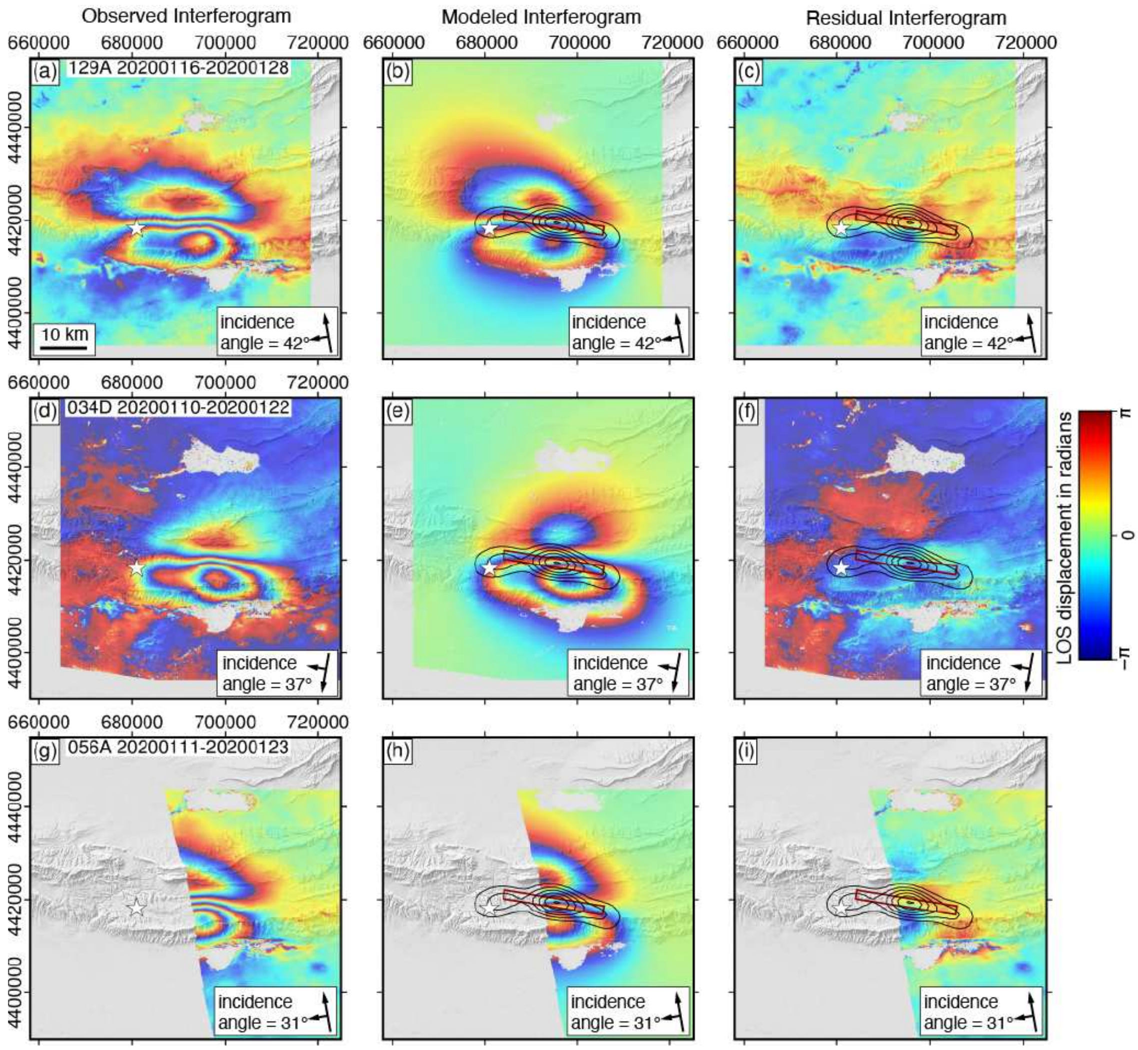


**Figure 2.** (Left column) Observed, (center) distributed slip model and (right) residual interferograms of the 2020 Jiashi mainshock rupture. Modelling was performed using unwrapped LOS displacements, but here we plot the original, wrapped (filtered) interferograms since these show more clearly the shape of the deformation field. The coordinates are in UTM 43N. Color cycles of blue through yellow to red indicate motion away from the satellite and one color cycle ($2\pi$ radians) represents a half radar wavelength (2.8 cm) of LOS displacement. The satellite track azimuths and LOS direction with local angle of incidence are indicated by the longer and shorter black arrows, respectively. The white star indicates the relocated mainshock epicenter. In the central and right-hand panels, ten centimeter model slip contours are shown in black and the outline of the uniform slip model fault plane is marked in dark red.

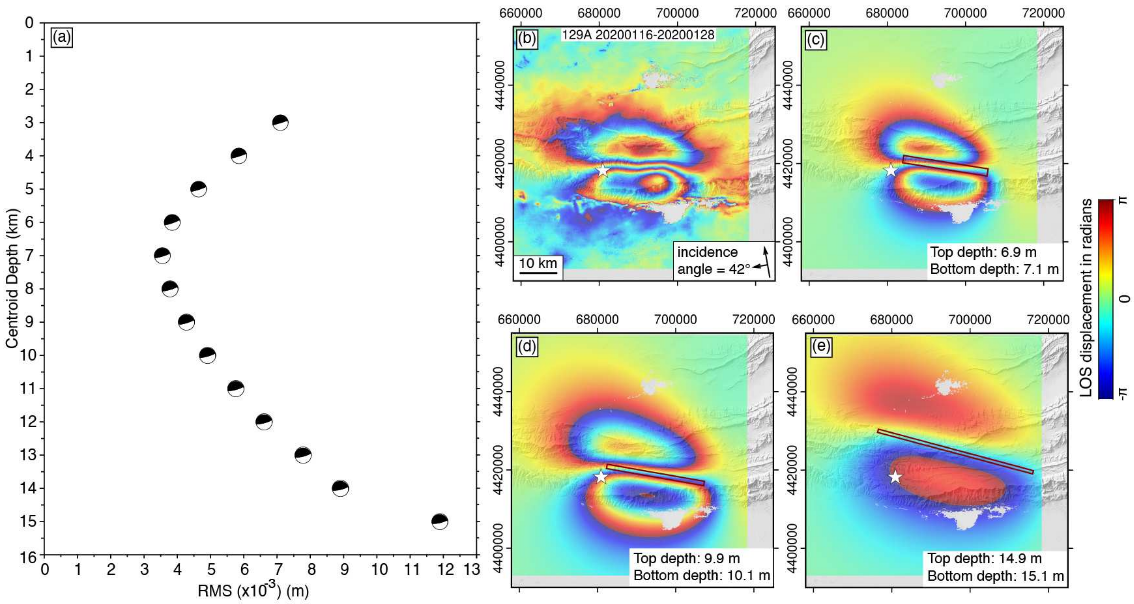


**Figure 3.** (a) Fault center depth sensitivity tests of our InSAR uniform slip fault models for the 2020 Jiashi mainshock. Each focal mechanism shows the minimum-misfit model solution for a fixed center depth, with all other parameters kept free in each inversion. The $x$-axis is root mean square error (RMS) in meters; the $y$ axis shows 1 km increments of fixed center depth. (b) Observed ascending track interferogram (same as in Fig. 2a). (c) Preferred uniform slip model interferogram, with its (free) center depth of 7 km. (d) A forward model interferogram with center depth fixed to 10 km. The forward model used the same uniform slip parameters as in (c) except for the top and bottom depth and the surface projection coordinates. (e) Same as (d) but with a centroid depth of 15 km. The coordinates are in UTM 43N.

mainshock slip resolved by InSAR inversion. We consider two possible explanations for this apparent discrepancy.

The first possible explanation is that the surface deformation captured with InSAR may reflect aseismic afterslip along the décollement, above an earthquake buried within the underlying basement (at the depth of the aftershock concentration) and itself invisible to InSAR. We tested this possibility by forward modelling the interferograms based upon a $M_w$ 6.0 thrust earthquake with the same geometry as our preferred uniform slip model fault but centered at depths of 10 km and 15 km, more consistent with the aftershock seismicity (Fig. 3c, d). These forward model interfer-

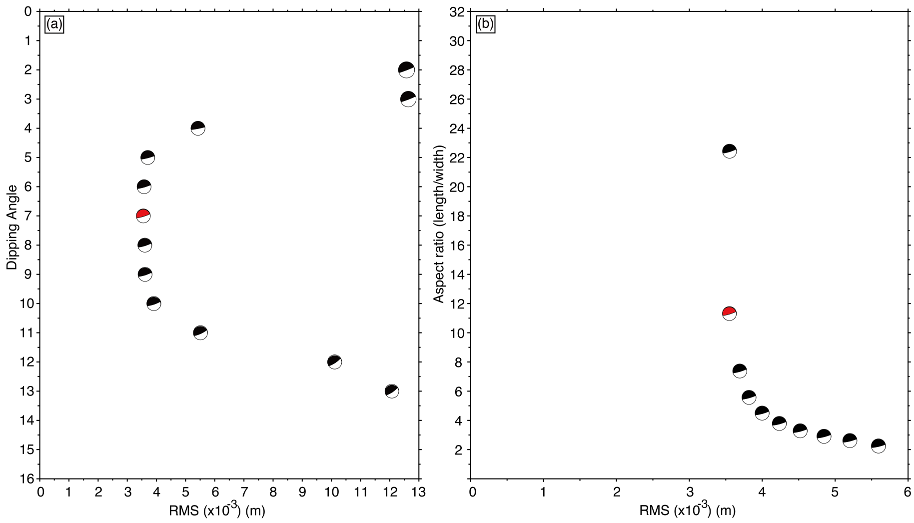


**Figure 4.** (a) Fault dip sensitivity tests of our InSAR uniform slip fault models for the 2020 Jiashi mainshock. Each focal mechanism shows the minimum-misfit model solution for a fixed dip angle, with all other parameters kept free in each inversion. The $x$-axis is root mean square error (RMS) in meters; the $y$ axis shows $1^\circ$ increments of fixed dip. The one with red compression part indicates the optimal uniform slip model. (b) Fault plane width sensitivity tests. Each focal mechanism shows the minimum-misfit model solution for a fixed fault width (obtained by fixing the centroid depth and dip to the minimum misfit values and extending the fault plane up- and down-dip at 1 kilometer increments). All other parameters, including slip and fault length, are allowed to vary and the results are plotted according to the aspect ratio of length to width. The red focal mechanism indicates the optimal uniform slip model.

ograms match poorly with the observed InSAR data, with noticeably more far-field deformation and a broader spacing of fringes between the southern and northern lobes. However, the fact that this surface deformation remains distinguishable leads us to rule out the possibility that coseismic slip is too deep to be resolved with InSAR.

The second possible explanation is that the InSAR captures mainshock slip but that well-located aftershocks are vertically separated from the mainshock within the underlying basement, perhaps concentrated within a lobe of positive Coulomb stress change expected below the base of a thrust or reverse fault (e.g. Lin & Stein, 2004; Zhou et al., 2019). He et al. (2021) showed that double-difference relocated aftershocks concentrate along two steep planes within the basement; they then used Coulomb stress calculations to estimate the kinematics of these faults most

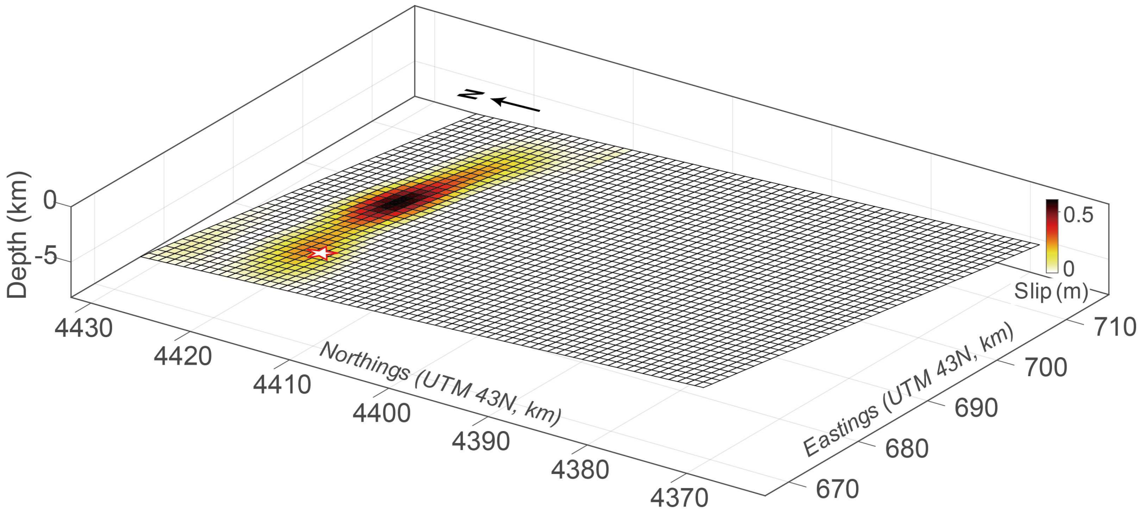


**Figure 5.** The perspective view of the coseismic slip distribution. The fault plane dips to north shallowly. Significant slip occurs over the depth range 6.5–7.4 km. The red star marks the relocated epicenter near the western end of the deformation field for the 2020 Jiashi earthquake.

consistent with static stress triggering by the shallower mainshock. This implies that the basement aftershocks involved N–S-oriented sinistral and steep, S-dipping reverse faulting. However, this does not explain the absence of shallow aftershocks within positive Coulomb stress lobes expected above the top mainshock fault edge. This might reflect an effect on the stress field from the stress-free boundary of the Earth's surface, that the faults within the sediments above the décollement may exhibit velocity-strengthening friction, favouring aseismic creep over seismic slip (Karasözen et al., 2016), or that the seismic network is insensitive to shallow events due to its average station spacing of $\sim$30 km. Local seismic networks are able to constrain the focal depth most accurately only if *Pg* and *Sg* phases are recorded at epicentral distances of less than $\sim$1–2 times of focal depths and the average station spacing is also less than $\sim$1–2 times of focal depths (Gomberg et al., 1990). Therefore, the apparent absence of shallow events may be an artefact, as the stations with average spacing of $\sim$30 km cannot record aftershocks shallower than 15 km depth.

We agree with the explanation favored by He et al. (2021) that the mainshock and aftershocks are vertically separated, as our teleseismic waveform inversion reinforces that the geodetically-

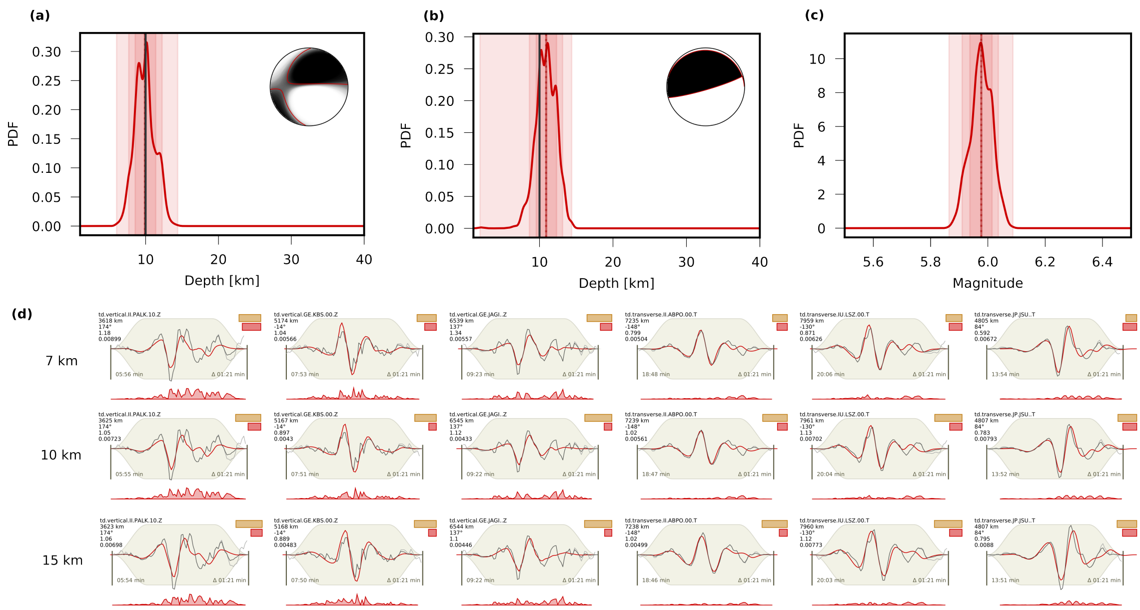


**Figure 6.** Seismological processing results for the 2020 Jiashi mainshock. (a) Probability-density function for depth, for an inversion with all parameters free. Inset mechanism shows the mechanism probability density function (greys) and the best-fit solution (red). (b) Probability-density function for depth, for an inversion with the mechanism constrained to be a double couple matching the InSAR-derived fault plane. (c) Probability-density function for moment, for an inversion with the mechanism constrained to match the InSAR-derived fault plane. (d) Example waveforms for 6 stations (three vertical component, three transverse component). Black traces show the observed data, red line shows the best-fitting inversion result. Text on each waveform indicates the station and component, epicentral distance, and azimuth. Each row of waveforms show synthetics calculated at 7, 10, and 15 km respectively, as discussed in the text.

imaged signal is indeed coseismic. The waveform misfit differences between depths of 10 km and 7 km are minimal (Fig. 6d). However, synthetics are notably too broad at all six of the stations shown when the depth is increased to 15 km. Due to the cross-correlation based alignment, synthetics are typically aligned on the dominant peak to minimise misfit. However, at 15 km depth, this leads to the peaks to either side being too far out from the main peak due to the increase separation between direct and depth phases. Thus, we conclude that the seismological data are consistent with the deformation signal detected using InSAR, but are notably shallower than the aftershocks located using regional seismology.

Mainshock–aftershock depth discrepancies are not uncommon and several other earthquake sequences also exhibit similar characteristics. The 2000 $M_w$ 6.6 Torrori (Japan), 2003 $M_w$ 6.6 Bam (Iran), 2008 $M_w$ 7.9 Wenchuan (China), 2009 $M_w$ 5.9 Karonga (Malawi), 2011 $M_w$ 5.9 Simav (Turkey), and 2014 $M_w$ 6.1 South Napa (California) earthquakes all exhibited shallower mainshock slip, resolved mostly using geodesy, with deeper aftershock distributions, resolved using seismology (Semmane et al., 2005; Jackson et al., 2006; Tong et al., 2010; Wei et al., 2015; Karasözen et al., 2016; Gaherty et al., 2019). Similar patterns were also observed in $M_w$ ∼6 earthquakes and aftershock sequences at Qeshm (2005) and Fin (2006) in the Zagros Simply Folded Belt, Iran (Nissen et al., 2010; Roustaei et al., 2010). These are especially analogous to the Jiashi sequence, as the Zagros mainshocks were centered within a thick sedimentary cover, with aftershock microseismicity vertically separated within the underlying basement (Nissen et al., 2014). Finally, we recollect that the February 24, 2003 $M_w$ 6.2 Jiashi earthquake in the foreland basin south of the Kepingtag was centered at ∼5–7 km depth, but exhibited aftershocks at ∼15–25 km depth (Huang et al., 2006; Sloan et al., 2011).

## 5.2 Structural interpretation of the 2020 Jiashi rupture

Coseismic uplift in the 2020 $M_w$ 6.0 Jiashi earthquake resolved by InSAR is centered along the back limb of the Kepingtag anticline (Fig. 7a–d). Seismic reflection profiles and balanced geological cross-sections depict this as a fault-propagation fold, with Paleozoic-Mesozoic sediments thrust over Cenozoic strata along the moderately northward-dipping Kepingtag fault, which branches off a décollement with an estimated depth of ∼5–10 km (Yin et al., 1998; Allen et al., 1999; Yang et al., 2010, 2002). Projecting our slip model onto a modified geological cross-section suggests that the 2020 earthquake ruptured the décollement where it intersects with the base of the Kepingtag thrust fault (Fig. 7e).

A striking feature of our distributed slip model is its elongate shape, with a length-to-width aspect ratio of greater than 4 (Fig. 5). This indicates that the earthquake was able to propagate readily along strike, but was prevented from doing so up- and down-dip. We consider two potential causes of this pattern. One possibility is that the stratigraphic configuration could have determined where slip was able to propagate, with rupture restricted to competent rocks such as the lowermost Cambrian limestone. A similar explanation was proposed by Elliott et al. (2015) for the elongate slip distribution (length-to-width ratio $\sim$3) of the 2013 $M_w$ 6.2 Khaki-Shonbe earthquake in the Zagros fold-and-thrust belt, where Infracambrian Hormuz evaporites and Cretaceous Kazhdumi mudstones were inferred to have controlled the bottom and top of the rupture, respectively. Length-to-width ratios of $\sim$3–4 inferred for the 2006 Fin and 2019 Khalili earthquakes (both $M_w$ 5.7) suggest that this may be a common feature of Zagros ruptures (Roustaei et al., 2010; Jamalreyhani et al., 2021). Another possible mechanism could be due to structural complexities in the fault geometry. This was discussed by Elliott et al. (2011) for the 2008 and 2009 Qaidam $M_w$ 6.3 earthquakes, whose vertical segregation resulted from disruption of the rupture plane by a cross-cutting, conjugate reverse fault. In the 2020 Jiashi event, we suggest that the abrupt change in dip angle between the sub-horizontal décollement and the much steeper Kepingtag fault may have provided a barrier to rupture. Our testing of listric fault geometries is in good agreement with the inference that there was minimal slip on the steeper fault. Although the current data does not allow us to distinguish between the two mechanisms, there is a clear structural or lithological control on the extent of coseismic slip during the mainshock.

### 5.3 Regional distribution of seismicity and seismic hazard

The Pamir and Tian Shan jointly accommodate a crustal shortening of 20–25 mm/yr, nearly half of the total India-Eurasia convergence rate (Abdrakhmatov et al., 1996; Zubovich et al., 2010). The southwestern margin of the Tian Shan is characterized by frequent seismicity, mostly with thrust faulting and strike-slip mechanisms. Here, we use our own calibrated earthquake relocations together with previous waveform modelling studies to assess the finer-scale distribution of seismicity across this region.

From the calibrated earthquake relocations, it is apparent that seismicity is not concentrated along the frontal Kepingtag belt, but is distributed throughout the fold-and-thrust belt as well as the adjacent foreland to the south. The shallow events occur to the north of the frontal Kepingtag anticline as well as in the foreland to the south. This pattern indicates that all stacks of the thrust

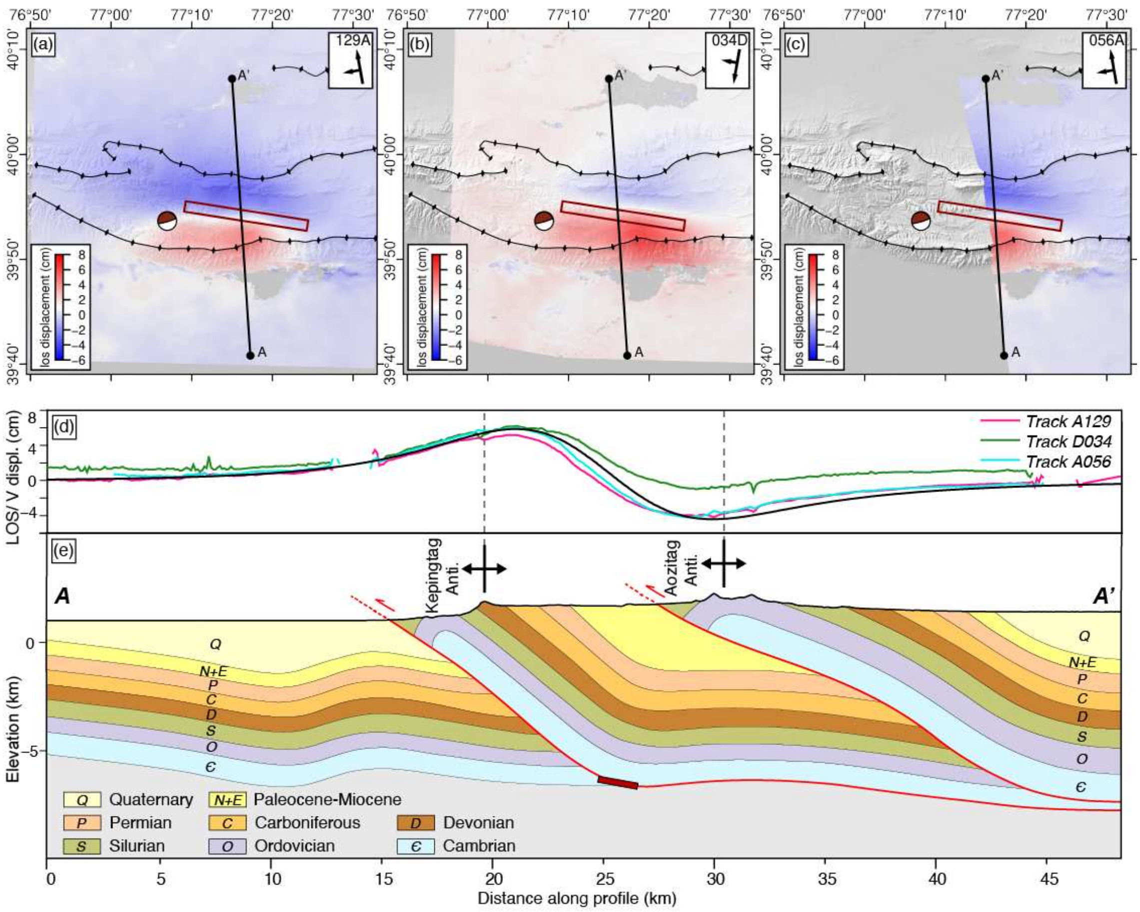


**Figure 7.** Coseismic LOS displacements in the 2020 Jiashi earthquake from unwrapped interferograms on tracks (a) 129A, (b) 034D and (c) 056A. Black lines with ticks show the traces of the Aozitang (north) and Kepingtag (south) fold axes. The dark red rectangle is the uniform slip model fault plane, centered at ∼7 km depth. (d) LOS displacement profiles and vertical displacement profile (track A129 in pink, D034 in green, A056 in cyan, and vertical displacement in black) along profile A-A' in (a), (b) and (c). Maximum LOS displacements are ∼7.5 cm toward the satellite and ∼4 cm away from the satellite. Vertical displacement field is predicted by our best fitting, InSAR-derived distributed slip model. (e) Geological cross-section along the profile A-A', interpreted from seismic reflection profiles (Yang et al., 2010). The surface topography is extracted from the 30 m resolution SRTM DEM. The dark red rectangle indicates the uniform slip model fault plane.

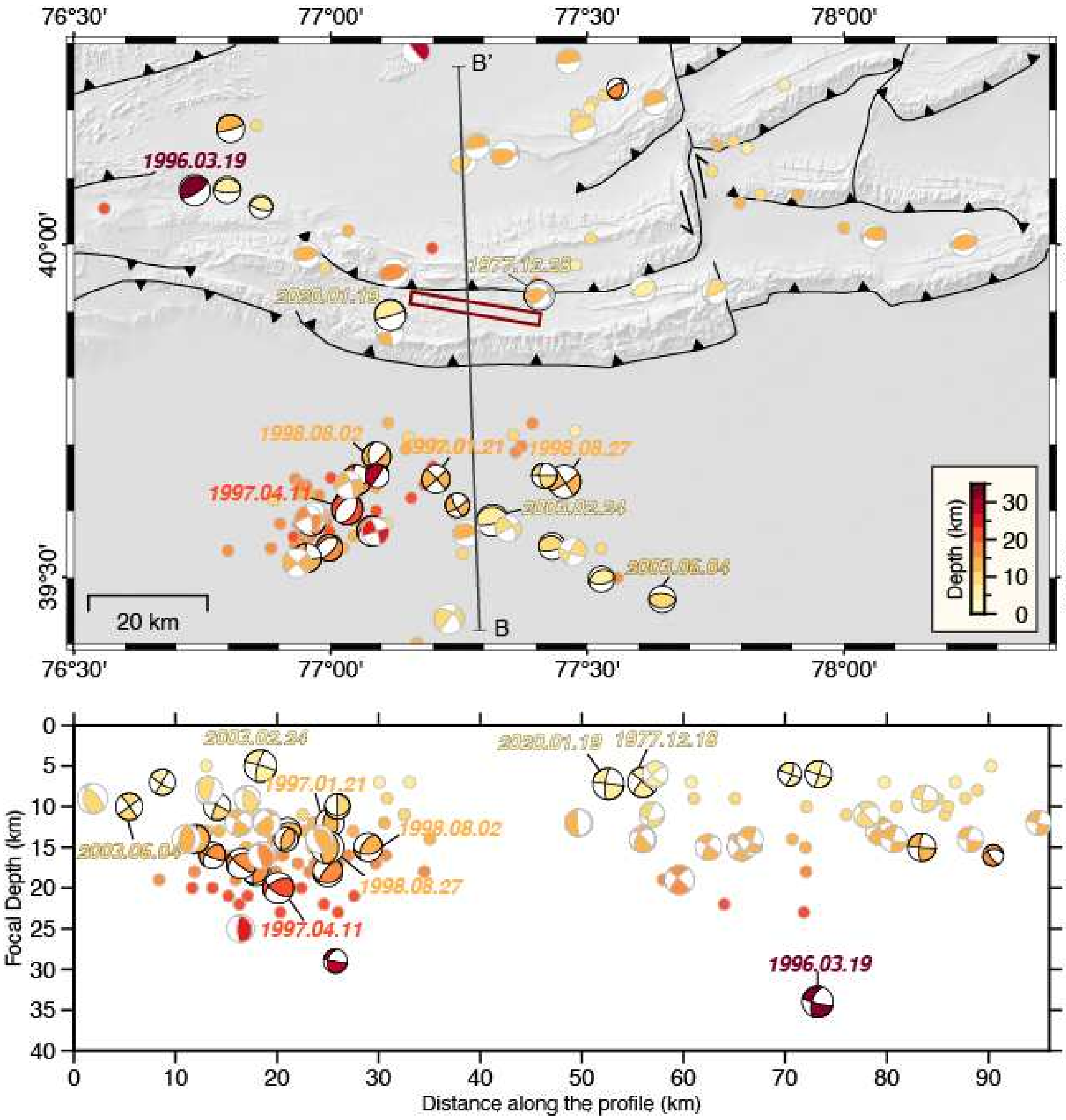


**Figure 8.** Calibrated relocated earthquakes from 1977–2020 in the Jiashi area, coloured according to the best available estimate of depth. Focal mechanisms determined by teleseismic and regional waveform modelling, including some from the GCMT catalogue. The depths of focal mechanisms with black outlines are determined by teleseismic and regional waveform modelling and depth phases, while those with grey outlines are our own calibrated focal depths (see Table 2 for full details). Other moderate relocated earthquakes without focal mechanisms are shown as dots.

sheets may be simultaneously capable of generating earthquakes, even as one of them might be most favourable at a particular time due to a variable stress state and the history of previous earthquakes. This inference is also supported by geomorphological and geochronological data (Yang et al., 2006) and suggests that seismic hazard is high across the region, rather than being focused along the range front.

Moreover, the seismic hazard in the Kepingtag region is not only restricted to faulting along the décollement but also within the folded cover rocks and the piedmont area. Reliable earthquake centroid and focal depths — from teleseismic or regional waveform modelling (Fan et al., 1994; Ghose et al., 1998; Sloan et al., 2011) and our own calibrated hypocentral relocations — are concentrated at depths shallower than 25 km, except for two isolated events at 29–35 km (Fig. 8). The 1997 Jiashi earthquake swarm and the 2003 Bachu-Jiashi sequence all occurred on blind faults in the piedmont area $\sim$50 km south of the Kepingtag frontal thrust. The largest events between 1997 and 1998 ($M_w$ 5.7, 5.9, 6.0 and 6.3) represented activity on normal faulting or left-lateral strike-slip faulting at mid-crustal depths of $\sim$12–20 km, while the 2003 events involved much shallower thrust faulting (Sloan et al., 2011). Within the Kepingtag fold-and-thrust belt, most of the reliable centroid depths are greater than 10 km, indicating faulting within the basement is below the décollement. Though usually depicted as a 'thin-skinned' fold-and-thrust belt, the Kepingtag basement clearly accommodates shortening by reverse faulting, and should therefore be considered as an important source of seismic hazard.

## 6 CONCLUSION

We use InSAR data to characterize the coseismic surface deformation and model the fault geometry and slip distribution of the January 19 2020 $M_w$ 6.0 Jiashi earthquake. Modelled coseismic uplift is centered on the back limb of the Kepingtag anticline, consistent with previous structural models that depict this as a fault-propagation fold. Our best-fit model fault plane dips $\sim$7° northward at depth of $\sim$7 km, placing it on or close to the mapped décollement at the base of the folded sedimentary cover. This depth is consistent with teleseismic body-waveforms, confirming that the slip modelled with InSAR occurred coseismically. The small ($\sim$1/4) width to length ratio of our model slip distribution hints at structural and/or lithological controls on slip propagation; for example, rupture may have been prevented from advancing up-dip by the abrupt change of dip angle between the sub-horizontal décollement and the much steeper Kepingtag thrust. Published seismological studies show that aftershocks cluster within underlying basement rocks at $\sim$10–20 km depth, vertically separated from the mainshock slip. Our own relocated background seismicity also shows a prevalence of seismicity at basement depths throughout the Kepingtag belt and its foreland, hinting at rheological controls on the depths at which earthquakes occur.

## ACKNOWLEDGMENTS

S. W. was supported by the China Scholarship Council and a Graduate Award from University of Victoria. E. N. and R. J. were funded separately by the Natural Science and Engineering Research Council of Canada (NSERC), the Canada Foundation for Innovation (CFI) and the BC Knowledge Develoment Fund (BCKDF). E. N. also acknowledges support from a Canada Research Chair. T. C. was supported by the Royal Society (UK) under URF\R1\180088. T. C. was also supported through COMET, the UK Natural Environment Research Council's Centre for the Observation and Modelling of Earthquakes, Volcanoes, and Tectonics. We are grateful to two anonymous reviewers for their constructive comments which significantly improve the manuscript.

## Data availability

Interferograms were constructed using Copernicus Sentinel-1 data (2020) available from https://scihub.copernic and processed in GAMMA software (https://www.gamma-rs.ch/). InSAR modelling codes are available from E. N. upon request. Earthquakes were relocated using $Mloc$ software (https://seismo.com/mloc/) using starting location parameters from the International Seismological Centre Bulletin (http://www.isc.ac.uk/i Full calibrated relocation results will be posted to the USGS ScienceBase website for the Global Catalog of Calibrated Earthquake Locations (GCCEL) (https://www.sciencebase.gov/catalog/item/59fb91fde4b0531197b16ac7). We also used focal mechanism data from the Global Centroid Moment Tensor project (https://www.globalcmt.org/). Several of the figures in the paper were plotted using Generic Mapping Tools (Wessel et al., 2019).

## References


Abdrakhmatov, K. Y., Aldazhanov, S. A., Hager, B. H., Hamburger, M. W., Herring, T. A., Kalabaev, K. B., Makarov, V. I., Molnar, P., Panasyuk, S. V., Prilepin, M. T., Reilinger, R. E., Sadybakasov, I. S., Souter, B. J., Trapeznikov, Y. A., Tsurkov, V. Y., & Zubovich, A. V., 1996. Relatively recent construction of the Tien Shan inferred from GPS measurements of present-day crustal deformation rates, *Nature*, **384**(6608), 450–453.

Ainscoe, E. A., Elliott, J. R., Copley, A., Craig, T. J., Li, T., Parsons, B. E., & Walker, R. T., 2017. Blind Thrusting, Surface Folding, and the Development of Geological Structure in the Mw 6.3 2015 Pishan (China) Earthquake, *Journal of Geophysical Research: Solid Earth*, **122**(11), 9359–9382.

Allen, M. B., Vincent, S. J., & Wheeler, P. J., 1999. Late Cenozoic tectonics of the Kepingtage thrust zone: Interactions of the Tien Shan and Tarim Basin, northwest China, *Tectonics*, **18**(4), 639–654.

Avouac, J. P. & Tapponnier, P., 1993. Kinematic model of active deformation in central Asia, *Geophysical Research Letters*, **20(10)**(10), 895–898.

Bayasgalan, A., Jackson, J., & McKenzie, D., 2005. Lithosphere rheology and active tectonics in mongolia: relations between earthquake source parameters, gravity and gps measurements, *Geophysical Journal International*, **163**(3), 1151–1179.

Beckers, J. & Lay, T., 1995. Very broadband seismic analysis of the 1992 Flores, Indonesia, earthquake ($M_w$ = 7.9), *Journal of Geophysical Research: Solid Earth*, **100**(B9), 18,179–18,193.

Bergman, E. A., Benz, H, M., Yeck, W. L., Karasözen, E., Engdahl, E. R., Ghods, A., Hayes, G. P., & Earle, P. S., submitted. A Global Catalog of Calibrated Earthquake Locations, *Geophysical Journal International*.

Bie, L., Ryder, I., Nippress, S. E. J., & Bürgmann, R., 2014. Coseismic and post-seismic activity associated with the 2008 $M_w$ 6.3 Damxung earthquake, Tibet, constrained by InSAR, *Geophysical Journal International*, **196**(2), 788–803.

Bro, R. & De Jong, S., 1997. A fast non-negativity-constrained least squares algorithm, *Journal of Chemometrics*, **11**(5), 393–401.

Burchfiel, B. C., Brown, E. T., Qidong, D., Xianyue, F., Jun, L., Molnar, P., Jianbang, S., Zhangming, W., & Huichuan, Y., 1999. Crustal shortening on the margins of the tien shan, Xinjiang, China, *International Geology Review*, **41**(8), 665–700.

Chen, J., Ran, Y., Yang, X., & Xu, X., 2006. Character of Late Quaternary activity of the east segment of the front-edge faults of Kalpintag, *Seismology and Geology*, **28**(2), 258–268 (in Chinese with English abstract).

Chounet, A., Vallée, M., Causse, M., & Courboulex, F., 2018. Global catalog of earthquake rupture velocities shows anticorrelation between stress drop and rupture velocity, *Tectonophysics*, **733**, 148–158.

Copley, A., 2014. Postseismic afterslip 30 years after the 1978 Tabas-e-Golshan (Iran) earthquake: observations and implications for the geological evolution of thrust belts, *Geophysical Journal International*, **197**(2), 665–679.

Copley, A., Karasozen, E., Oveisi, B., Elliott, J. R., Samsonov, S., & Nissen, E., 2015. Seismogenic faulting of the sedimentary sequence and laterally variable material properties in the Zagros Mountains (Iran) revealed by the August 2014 Murmuri (E. Dehloran) earthquake sequence, *Geophysical Journal International*, **203**(2), 1436–1459.

Davis, T. L., Namson, J., & Yerkes, R. F., 1989. A cross section of the Los Angeles area: seismically active fold and thrust belt, the 1987 Whittier Narrows earthquake, and earthquake hazard, *Journal of Geophysical Research*, **94**(B7), 9644–9664.

Elliott, J. R., Parsons, B., Jackson, J. A., Shan, X., Sloan, R. A., & Walker, R. T., 2011. Depth segmentation of the seismogenic continental crust: The 2008 and 2009 Qaidam earthquakes, *Geophysical Research Letters*, **38**(6), 1–6.

Elliott, J. R., Copley, A. C., Holley, R., Scharer, K., & Parsons, B., 2013. The 2011 Mw 7.1 Van (Eastern Turkey) earthquake, *Journal of Geophysical Research (Solid Earth)*, **118**(4), 1619–1637.

Elliott, J. R., Bergman, E. A., Copley, A. C., Ghods, A. R., Nissen, E. K., Oveisi, B., Tatar, M., Walters, R. J., & Yamini-Fard, F., 2015. The 2013 Mw 6.2 Khaki-Shonbe (Iran) Earthquake: Insights into seismic and aseismic shortening of the Zagros sedimentary cover, *Earth and Space*

*Science*, **2**(11), 435–471.

Elliott, J. R., Walters, R. J., & Wright, T. J., 2016. The role of space-based observation in understanding and responding to active tectonics and earthquakes, *Nature Communications*, **7**, 13844.

Engdahl, R. E., Jackson, J. A., Myers, S. C., Bergman, E. A., & Priestley, K., 2006. Relocation and assessment of seismicity in the Iran region, *Geophysical Journal International*, **167**(2), 761–778.

Fan, G., Ni, J. F., & Wallace, T. C., 1994. Active tectonics of the Pamirs and Karakorum, *Journal of Geophysical Research*, **99**(B4), 7131.

Funning, G. J., Parsons, B., Wright, T. J., Jackson, J. A., & Fielding, E. J., 2005. Surface displacements and source parameters of the 2003 Bam (Iran) earthquake from Envisat advanced synthetic aperture radar imagery, *Journal of Geophysical Research: Solid Earth*, **110**(B9), B09406.

Gaherty, J. B., Zheng, W., Shillington, D. J., Pritchard, M. E., Henderson, S. T., Chindandali, P. R., Mdala, H., Shuler, A., Lindsey, N., Oliva, S. J., Nooner, S., Scholz, C. A., Schaff, D., Ekström, G., & Nettles, M., 2019. Faulting processes during early-stage rifting: Seismic and geodetic analysis of the 2009-2010 Northern Malawi earthquake sequence, *Geophysical Journal International*, **217**(3), 1767–1782.

Gao, R., Hou, H., Cai, X., Knapp, J. H., He, R., Liu, J., Xiong, X., Guan, Y., Li, W., Zeng, L., & Roecker, S. W., 2013. Fine crustal structure beneath the junction of the southwest Tian Shan and Tarim Basin, NW China, *Lithoshere*, **5**(4), 382–392.

Gaudreau, É., Nissen, E., Bergman, E. A., Benz, H. M., Tan, F., & Karasözen, E., 2019. The August 2018 Kaktovik earthquakes: Active tectonics in northeastern Alaska revealed with InSAR and seismology, *Geophysical Research Letters*, **46**(24), 14412–14420.

Ghose, S., Hamburger, M. W., & Ammon, C. J., 1998. Source parameters of moderate-sized earthquakes in the Tien Shan, central Asia from regional moment tensor inversion, *Geophysical Research Letters*, **25**(16), 3181–3184.

Goldstein, R. M., Zebker, H. A., & Werner, C. L., 1988. Satellite radar interferometry: Two-dimensional phase unwrapping, *Radio Science*, **23**(4), 713–720.

Gomberg, J. S., Shedlock, K. M., & Roecker, S. W., 1990. The effect of S-wave arrival times on the accuracy of hypocenter estimation, *Bulletin of the Seismological Society of America*, **80**(6A), 1605–1628.

He, Y., Wang, T., Fang, L., & Zhao, L., 2021. The 2020 Mw 6.0 Jiashi Earthquake: Coinvolvement of Thin-Skinned Thrusting and Basement Shortening in Shaping the Keping-Tage Fold-and-Thrust Belt in Southwestern Tian Shan, *Seismological Research Letters*.

Heimann, S., Isken, M., Kühn, D., Sudhaus, H., Steinberg, A., Daout, S., Cesca, S., Bathke, H., & Dahm, T., 2018. Grond: A probabilistic earthquake source inversion framework.

Hendrix, M. S., Graham, S. A., Carroll, A. R., Sobel, E. R., McKnight, C. L., Schulein, B. J., & Wang, Z., 1992. Sedimentary record and climatic implications of recurrent deformation in the Tian Shan: evidence from Mesozoic strata of the north Tarim, south Junggar, and Turpan basins, northwest China, *Geological Society of America Bulletin*, **104**(1), 53–79.

Huang, Y., Yang, J. S., & Zhang, T. Z., 2006. Relocation of the Bachu-Jiashi, Xinjiang earthquake sequence in 2003 using the double-difference location algorithm, *Acta Geophysica Sinica*, **49**(1), 162–169.

Jackson, J., Bouchon, M., Fielding, E., Funning, G., Ghorashi, M., Hatzfeld, D., Nazari, H., Parsons, B., Priestley, K., Talebian, M., Tatar, M., Walker, R., & Wright, T., 2006. Seismotectonic, rupture process, and earthquake-hazard aspects of the 2003 December 26 Bam, Iran, earthquake, *Geophysical Journal International*, **166**(3), 1270–1292.

Jamalreyhani, M., Pousse-Beltran, L., Büyükakpınar, P., Cesca, S., Nissen, E., Ghods, A., López-Comino, J. Á., Rezapour, M., & Najafi, M., 2021. The 2019-2020 Khalili (Iran) Earthquake Sequence—Anthropogenic Seismicity in the Zagros Simply Folded Belt?, *Journal of Geophysical Research (Solid Earth)*, **126**(12), e22797.

Jones, L., Aki, K., Boore, D., Celebi, M., Donnellan, A., Hall, J., Harris, R., Hauksson, E., Heaton, T., Hough, S., Hudnut, K., Hutton, K., Johnston, M., Joyner, W., Kanamori, H., Marshall, G., Michael, A., Mori, J., Murray, M., Ponti, D., Reasenberg, P., Schwartz, D., Seeber, L., Shakal, A., Simpson, R., Thio, H., Tinsley, J., Todorovska, M., Trifunac, M., Wald, D., & Zoback, M. L., 1994. The magnitude 6.7 Northridge, California, earthquake of 17 January 1994, *Science*, **266**(5184), 389–397.

Jónsson, S., Zebker, H., Segall, P., & Amelung, F., 2002. Fault slip distribution of the 1999 Mw 7.1 Hector Mine, California, earthquake, estimated from satellite radar and GPS measurements, *Bulletin of the Seismological Society of America*, **92**(4), 1377–1389.

Jordan, T. H. & Sverdrup, K. A., 1981. Teleseismic location techniques and their application to earthquake clusters in the South-Central Pacific, *Bulletin of the Seismological Society of America*, **71**, 1105–1130.

Karasözen, E., Nissen, E., Bergman, E. A., Johnson, K. L., & Walters, R. J., 2016. Normal faulting in the Simav graben of western Turkey reassessed with calibrated earthquake relocations, *Journal of Geophysical Research: Solid Earth*, **121**(6), 4553–4574.

Karasözen, E., Nissen, E., Büyükakpınar, P., Cambaz, M. D., Kahraman, M., KalkanÂ Ertan, E., Abgarmi, B., Bergman, E., Ghods, A., & Özacar, A. A., 2018. The 2017 July 20 $M_w$ 6.6 Bodrum-Kos earthquake illuminates active faulting in the Gulf of Gökova, SW Turkey, *Geophysical Journal International*, **214**(1), 185–199.

Karasözen, E., Nissen, E., Bergman, E. A., & Ghods, A., 2019. Seismotectonics of the Zagros (Iran) From Orogen-Wide, Calibrated Earthquake Relocations, *Journal of Geophysical Research: Solid Earth*, **124**(8), 9109–9129.

Kennett, B. L. N., Engdahl, E. R., & Buland, R., 1995. Constraints on seismic velocities in the Earth from traveltimes, *Geophysical Journal International*, **122**(1), 108–124.

Kulikova, G. & Krüger, F., 2017. Historical seismogram reproductions for the source parameters determination of the 1902, Atushi (Kashgar) earthquake, *Journal of Seismology*, **21**(6), 1577–1597.

Li, S. & Barnhart, W. D., 2020. Impacts of Topographic Relief and Crustal Heterogeneity on Coseismic Deformation and Inversions for Fault Geometry and Slip: A Case Study of the 2015 Gorkha Earthquake in the Central Himalayan Arc, *Geochemistry, Geophysics, Geosystems*, **21**(12), e09413.

Lin, J. & Stein, R. S., 2004. Stress triggering in thrust and subduction earthquakes and stress interaction between the southern San Andreas and nearby thrust and strike-slip faults, *Journal* *of Geophysical Research (Solid Earth)*, **109**(B2), B02303.

Mallick, R., Bürgmann, R., Johnson, K., & Hubbard, J., 2021. A unified framework for earthquake sequences and the growth of geological structure in fold-thrust belts, *Journal of Geophysical Research: Solid Earth*.

Nishidai, T. & Berry, J. L., 1990. Structure and Hydrocarbon Potential of the Tarim Basin (Nw China) From Satellite Imagery, *Journal of Petroleum Geology*, **13**(1), 35–58.

Nissen, E., Ghorashi, M., Jackson, J., Parsons, B., & Talebian, M., 2007. The 2005 Qeshm Island earthquake (Iran) - A link between buried reverse faulting and surface folding in the Zagros Simply Folded Belt?, *Geophysical Journal International*, **171**(1), 326–338.

Nissen, E., Yamini-Fard, F., Tatar, M., Gholamzadeh, A., Bergman, E., Elliott, J. R., Jackson, J. A., & Parsons, B., 2010. The vertical separation of mainshock rupture and microseismicity at Qeshm island in the Zagros fold-and-thrust belt, Iran, *Earth and Planetary Science Letters*, **296**(3-4), 181–194.

Nissen, E., Tatar, M., Jackson, J. A., & Allen, M. B., 2011. New views on earthquake faulting in the Zagros fold-and-thrust belt of Iran, *Geophysical Journal International*, **186**(3), 928–944.

Nissen, E., Jackson, J., Jahani, S., & Tatar, M., 2014. Zagros ”phantom earthquakes” reassessed - The interplay of seismicity and deep salt flow in the Simply Folded Belt?, *Journal of Geophysical Research: Solid Earth*, **119**(4), 3561–3583.

Okada, Y., 1985. Surface deformation due to shear and tensile faults in a half-space, *Bulletin of the seismological society of America*, **75**(4), 1135–1154.

Pousse-Beltran, L., Nissen, E., Bergman, E. A., Cambaz, M. D., Gaudreau, É., Karasözen, E., & Tan, F., 2020. The 2020 $M_w$ 6.8 Elazığ (Turkey) Earthquake Reveals Rupture Behavior of the East Anatolian Fault, *Geophys. Res. Lett.,* , **47**(13), e88136.

Press, W. H., Flannery, B. P., Teukolsky, S. A., & Vetterling, W. T., 1992. Numeric recipes in C: the art of scientific computing, *Camb. Univ. Press Camb*.

Ran, H., Shangguan, W., & Liu, D., 2020. Location study of Xinjiang Jiashi Ms6.4 earthquake and aftershocks sequence on January 19th, 2020, *Inland Earthquake*, **34(1)**, 56–61.

Ran, Y., Yang, X., Xu, X., Cheng, J., & Chen, L., 2006. Deformation pattern and shortening rates in the east part of Kalpin Thrust system in southwest Tianshan during late Quaternary, *Seismology and Geology (in Chinese with English abstract)*, **28(2)**, 179–193.

Reigber, C., Michel, G. W., Galas, R., Angermann, D., Klotz, J., Chen, J. Y., Papschev, A., Arslanov, R., Tzurkov, V. E., & Ishanov, M. C., 2001. New space geodetic constraints on the distribution of deformation in Central Asia, *Earth and Planetary Science Letters*, **191**(1-2), 157–165.

Roustaei, M., Nissen, E., Abbassi, M., Gholamzadeh, A., Ghorashi, M., Tatar, M., Yamini-Fard, F., Bergman, E., Jackson, J., & Parsons, B., 2010. The 2006 March 25 Fin earthquakes (Iran)-insights into the vertical extents of faulting in the Zagros Simply Folded Belt, *Geophysical Journal International*, **181**(3), 1275–1291.

Semmane, F., Cotton, F., & Campillo, M., 2005. The 2000 Tottori earthquake: A shallow earthquake with no surface rupture and slip properties controlled by depth, *Journal of Geophysical Research: Solid Earth*, **110**(3), 1–13.

Sloan, R. A., Jackson, J. A., Mckenzie, D., & Priestley, K., 2011. Earthquake depth distributions in central Asia, and their relations with lithosphere thickness, shortening and extension, *Geophysical Journal International*, **185**(1), 1–29.

Tong, X., Sandwell, D. T., & Fialko, Y., 2010. Coseismic slip model of the 2008 Wenchuan earthquake derived from joint inversion of interferometric synthetic aperture radar, GPS, and field data, *Journal of Geophysical Research*, **115**(B4), 1–19.

Walker, R., Jackson, J., & Baker, C., 2003. Surface expression of thrust faulting in eastern Iran: source parameters and surface deformation of the 1978 Tabas and 1968 Ferdows earthquake sequences, *Geophysical Journal International*, **152**(3), 749–765.

Walker, R. T., Bergman, E. A., Szeliga, W., & Fielding, E. J., 2011. Insights into the 1968-1997 Dasht-e-Bayaz and Zirkuh earthquake sequences, eastern Iran, from calibrated relocations, InSAR and high-resolution satellite imagery, *Geophysical Journal International*, **187**(3), 1577–1603.

Wang, D., Zhao, B., Yu, J., & Tan, K., 2020. Active tectonic deformation around the Tarim Basin inferred from dense GPS measurements, *Geodesy and Geodynamics*, **11**(6), 418–425.

Wei, S., Barbot, S., Graves, R., Lienkaemper, J. J., Wang, T., Hudnut, K., Fu, Y., & Helmberger, D., 2015. The 2014 Mw 6.1 South Napa Earthquake: A unilateral rupture with shallow asperity and rapid afterslip, *Seismological Research Letters*, **86**(2A), 344–354.

Werner, C., Wegmüller, U., Strozzi, T., & Wiesmann, A., 2000. Gamma SAR and interferometric processing software, in *Proceedings of the ERS-ENVISAT symposium, Gothenburg, Sweden*.

Wessel, P., Luis, J., Uieda, L., Scharroo, R., Wobbe, F., Smith, W., & Tian, D., 2019. The generic mapping tools version 6, *Geochemistry, Geophysics, Geosystems*, **20**(11), 5556–5564.

Weston, J., Ferreira, A. M. G., & Funning, G. J., 2011. Global compilation of interferometric synthetic aperture radar earthquake source models: 1. Comparisons with seismic catalogs, *Journal of Geophysical Research: Solid Earth*, **116**(B8), B08408.

Wimpenny, S. & Scott Watson, C., 2020. gWFM: A global catalog of moderate-magnitude earthquakes studied using teleseismic body waves, *Seismological Research Letters*, **92**(1), 212–226.

Windley, B. F., Allen, M. B., Zhang, C., Zhao, Z. Y., & Wang, G. R., 1990. Paleozoic accretion and Cenozoic redeformation of the Chinese Tien Shan Range, central Asia.

Wright, T. J., Parsons, B. E., Jackson, J. A., Haynes, M., Fielding, E. J., England, P. C., & Clarke, P. J., 1999. Source parameters of the 1 October 1995 Dinar (Turkey) earthquake from SAR interferometry and seismic bodywave modelling, *Earth and Planetary Science Letters*, **172**(1-2), 23–37.

Wright, T. J., Lu, Z., & Wicks, C., 2004. Constraining the slip distribution and fault geometry of the Mw 7.9, 3 November 2002, Denali fault earthquake with Interferometric Synthetic Aperture Radar and Global Positioning System data, *Bulletin of the Seismological Society of America*, **94**(6 SUPPL. B), 175–189.

Xinjiang Bureau of Geology and Mineral Resources, 1993. *Regional Geology of Xinjiang Uygur Autonomous Region*, Geological Publishing House, Beijing.

Xu, Y., Roecker, S. W., Wei, R., Zhang, W., & Wei, B., 2006. Analysis of seismic activity in the crust from earthquake relocation in the central Tien Shan, *Bulletin of the Seismological Society of America*, **96**(2), 737–744.

Yang, H., Li, Y., Shi, J., Xiao, A., Huang, S., Wu, G., Wang, H., Wang, X., Zhao, Y., & Liu, Y., 2010. Tectonic characteristics of the Late Cenozoic south Tianshan fold-and-thrust belt, *Quaternary Sciences*, **30**(5), 1030–1043 (in Chinese with English abstract).

Yang, X., Ran, Y., Song, F., Xu, X., Cheng, J., Min, W., Han, Z., & Chen, L., 2006. The analysis for crust shortening of Kalpin Thrust tectonic zone, south-western Tianshan, Xinjiang, China, *Seismology and Geology (in Chinese with English abstract)*, **28**(2), 194–204.

Yang, Z. X., Zhao, J. R., Zhang, X. K., Zhang, C. K., Cheng, S. X., Duan, Y. L., Zhang, J. S., & Wang, S. J., 2002. Tomographic determination of the upper crustal structure in the Jiashi strong earthquake swarm region, *Acta Seismologica Sinica English Edition*, **15**(2), 162–170.

Yao, Q., Yang, W., Jiang, X., Guo, Y., Liu, J., Zhang, Y., Wang, H., Ren, J., Yu, C., Yue, C., & Zhao, J., 2021a. The 2020 M6.4 Jiashi Earthquake: An Event that Occurred Under the Décollement on the Kaping Fold-and-Thrust Belt in the Southwestern Tien Shan Mountains, China, *Frontiers in Earth Science*, **9**(May), 1–14.

Yao, Y., Wen, S., Li, T., & Wang, C., 2021b. The 2020 Mw6.0 Jiashi earthquake: A fold earthquake event in the southern Tian Shan, northwest China, *Seismological Research Letters*, **92**(2), 859–869.

Yin, A., Craig, P., Harrison, T. M., Ryerson, F. J., Qian, X., & Yang, G., 1998. Late Cenozoic tectonic evolution of the southern Chinese Tian Shan, *Tectonics*, **17**(1), 1–27.

Yu, P., Qiao, X., Xiong, W., Chen, W., Nie, Z., Wang, D., Jia, Z., & Li, J., 2020. Source model for the M w 6.0 earthquake in Jiashi, China on 19 January 2020 from Sentinel-1A InSAR data, *Earth, Planets and Space*, **72**(1).

Zhang, G., Zhu, L., Song, X., Li, Z., Yang, M., Su, N., & Chen, X., 1999. Predictions of the 1997 strong earthquakes in Jiashi, Xinjiang, China, *Bulletin of the Seismological Society of America*, **89**(5), 1171–1183.

Zhang, Z. Q., Chen, J. Y. S., & Lin, J., 2008. Stress interactions between normal faults and adjacent strike-slip faults of 1997 Jiashi earthquake swarm, *Science in China, Series D: Earth Sciences*, **51**(3), 431–440.

Zhou, S. Y. & Xu, Z. H., 2000. Fracture characteristics of the 1997 Jiashi, Xinjiang, China, earthquake swarm inferred from source spectra, *Acta Seismologica Sinica English Edition*, **13**(2), 125–135.

Zhou, Z., Kusky, T. M., & Tang, C.-C., 2019. Coulomb stress change pattern and aftershock distributions associated with a blind low-angle megathrust fault, Nepalese Himalaya, *Tectonophysics*, **767**, 228161.

Zubovich, A. V., Wang, X. Q., Scherba, Y. G., Schelochkov, G. G., Reilinger, R., Reigber, C., Mosienko, O. I., Molnar, P., Michajljow, W., Makarov, V. I., Li, J., Kuzikov, S. I., Herring, T. A., Hamburger, M. W., Hager, B. H., Dang, Y. M., Bragin, V. D., & Beisenbaev, R. T., 2010. GPS velocity field for the Tien Shan and surrounding regions, *Tectonics*, **29**(6), 1–23.